UNCLASSIFIED

DTIC FILE

②

ITY CLASSIFICATION OF THIS PAGE

REPORT DOCUMENTATIO

AD-A229 244

Approved
No. 0704-0188

EPORT SECURITY CLASSIFICATION
Unclassified

ECURITY CLASSIFICATION AUTHORITY
N/A

ECLASSIFICATION/DOWNGRADING SCHEDULE
N/A

3. DISTRIBUTION/AVAILABILITY OF REPORT
SBIR Phase II Final Report
Approved for public release,
distribution unlimited

ERFORMING ORGANIZATION REPORT NUMBER(S)
Contract F49620-89-C-0013

5. MONITORING ORGANIZATION REPORT NUMBER(S)
AFOSR/NA
AFOSR-TR- 90 1144

AME OF PERFORMING ORGANIZATION
IntelliSys Corporation

6b. OFFICE SYMBOL *(If applicable)*

7a. NAME OF MONITORING ORGANIZATION
AFOSR/NA

DDRESS (City, State, and ZIP Code)
IntelliSys Corporation
3801 Eubank NE, Suite 201
Albuquerque, NM 87111

7b. ADDRESS (City, State, and ZIP Code)
Air Force Office of Scientific Researc
AFOSR/NA
Bolling AFB, DC 20332

DTIC
ELECTE
NOV 21 1990
S D
C

AME OF FUNDING/SPONSORING ORGANIZATION
AFOSR

8b. OFFICE SYMBOL *(If applicable)*
NA

9. PROCUREMENT INSTRUMENT IDENTIFICATION NUMBER
Contract F49620-89-C-001

DDRESS (City, State, and ZIP Code)
AFOSR/NA
Bldg. 410, Bolling AFB, DC 20332

10. SOURCE OF FUNDING NUMBERS

PROGRAM ELEMENT NO.	PROJECT NO.	TASK NO.	WORK UNIT ACCESSION NO.
61102F	3005	A1	

ITLE *(Include Security Classification)*
Development of a High-Imaging Speed SEM for Dynamically Loaded Materials

ERSONAL AUTHOR(S)
Fishbine, B. H., Macy, R. J., Ross, T. J. and Wang, M. L.

TYPE OF REPORT
FINAL

13b. TIME COVERED
FROM Oct 1988 TO Oct 1990

14. DATE OF REPORT *(Year, Month, Day)*
31 October 1990

15. PAGE COUNT
57

UPPLEMENTARY NOTATION

COSATI CODES

FIELD	GROUP	SUB-GROUP

18. SUBJECT TERMS *(Continue on reverse if necessary and identify by block number)*
Scanning electron microscopy, shock, dynamic effects, fast scan, image resolution

BSTRACT *(Continue on reverse if necessary and identify by block number)*

During the research effort, the concept of using a high-speed scanning electron microscope (SEM) observe real-time microstructural response of dynamically loaded structural materials was verifi experimentally at a maximum framing rate of 381 Hz (256 horizontal pixels x 128 vertical pixels), about order of magnitude higher than previously possible with conventional SEM's. This experimen accomplishment proved the soundness of several key concepts: (1)That a tungsten hairpin cathode is brig enough to obtain useful digital images at the framing rate listed above; (2) that a secondary electr detector can be built and operated at high enough count rates to obtain such images; (3) that the scan c assembly standard on an ISI SX-40A SEM can be replaced to allow imaging at such rates with spat resolution approaching 100 nm; (4) that signal acquisition and scan generation can be synchronized obtain a succession of well-defined frames in a "movie" format at pixel rates far in excess of conventio TV-rate SEM video bandwidths; and (5) that a magnetically-induced stress wave device can be used obtain dynamic fracture within the SEM chamber and field of view, with scanning timed to coincide w fracture. Also documented herein are unanticipated results which occurred during the research period.

ISTRIBUTION/AVAILABILITY OF ABSTRACT
UNCLASSIFIED/UNLIMITED ☐ SAME AS RPT. ☐ DTIC USERS

21. ABSTRACT SECURITY CLASSIFICATION
Unclassified

NAME OF RESPONSIBLE INDIVIDUAL
SPENCER WU

22b. TELEPHONE (Include Area Code)
202-767-6962

22c. OFFICE SYMBOL
AFOSR/NA

orm 1473, JUN 86

Previous editions are obsolete.

SECURITY CLASSIFICATION OF THIS PAGE
Unclassified

UNCLASSIFIED

Final Report

AFOSR Phase II SBIR Project

Development of a High-Imaging Speed SEM
For Dynamically-Loaded Materials

B. H. Fishbine, R. J. Macy and T. J. Ross,
IntelliSys Corporation

and

M. L. Wang,
University of New Mexico

10/30/90

Table of Contents

I. Summary of Progress During the Research Effort

During the research effort, the concept of using a high-speed scanning electron microscope (SEM) to observe real-time microstructural response of dynamically loaded structural materials was verified experimentally at a maximum framing rate of 381 Hz (256 horizontal pixels X 128 vertical pixels), about an order of magnitude higher than previously possible with conventional SEM's. This experimental accomplishment proved the soundness of several key concepts outlined in the Phase II proposal [1]:

1. That a tungsten hairpin cathode is bright enough to obtain useful digital images at the framing rate listed above.

2. That a secondary electron detector can be built and operated at high enough count rates to obtain such images.

3. That the scan coil assembly standard on an ISI SX-40A SEM can be replaced to allow imaging at such rates with spatial resolution approaching 100 nm.

4. That signal acquisition and scan generation can be synchronized to obtain a succession of well-defined frames in a "movie" format at pixel rates far in excess of conventional TV-rate SEM video bandwidths.

5. That a magnetically-induced stress wave device can be used to obtain dynamic fracture within the SEM chamber and field of view, with scanning timed to coincide with fracture.

Some unanticipated results occuring during the research were:

1. The generation of eddy currents on the inner cylindrical surface of the SEM final lens pole piece reduced useful vertical pixel resolution from 256 to 128 and introduced slight vertical jitter in successive frames. There may also be astigmatic effects which may ultimately limit spatial resolution.

This problem is well-known in e-beam lithography and has been solved for fifteen or more years by magnetic shielding with high-frequency ferrite material [2]. It should be easy to use this technique in our system if magnetic deflection is pursued.

2. The tungsten hairpin gun in the SX-40A does not approach the theoretical brightness for such a gun [3], reducing the signal-to-noise ratio (S/N) and depth of focus available in digitized images. We have previously discussed the advantages of using a higher brightness gun [4]. Further significant development of this technology will require a brighter gun.

3. Practically, lower magnifications are essential to locate specimen features of interest in order to set up fracture or other dynamic experiments. In future experiments using magnetic deflection more attention should be directed to ways to reduce deflection coil heating effects.

4. If the electron source is adequate, the count rate of the detector determines the final image contrast range for a given pixel rate. A simple way to boost these values is to parallel several detectors [5].

5. The magnetically-induced stress wave concept for ~1 mm radius rod specimens allows for various combinations of dynamic loading--single- or double-ended, compression or tension--and does permit fracture to be localized within the SEM field of view and to time fracture with scanning. However, these advantages can only be realized for specimen materials which are homogeneous (on the scale of the pressure pulse length) and 1) can transmit a ~1 μs wide pressure pulse without dissipation, 2) are weak enough to break at pressure peaks in the 3,000-30,000 psi range (the present limits of our device extrapolated to the 35 kV maximum capacitor charge voltage) and 3) exhibit crack nucleation and growth and macroscopic fracture within ~1 μs.

In retrospect, our projections of 10-100 kHz framing rates in the Phase II proposal were probably too optimistic for a Phase II project because this means attaining framing rate improvements of several orders of magnitude above the state-of-the-art when this project was begun. However, we have solidly achieved one order of magnitude improvement, which has suitably impressed reviewers for two of the journals to which a paper describing early fast scan results has been submitted (Phys. Rev. Lett. and Rev. Sci. Instrum.). Rev. Sci. Instrum. has accepted the paper for publication [6].

We believe that >1 kHz digitally acquired framing rates are easily possible using commercial waveform synthesizers, but that imaging at such rates will be disappointing without attendant improvements in electron source brightness and secondary electron detector count rate. In fact we have obtained analog-acquired images at effective framing rates of 4.9 kHz, with good image sharpness and linearity at high magnification but restricted contrast range. With the suggested source and detector improvements we are hopeful that future research will permit us to obtain good digital images at framing rates well in excess of 1 kHz. Based on current technology, feasibility has been indicated for ~500 kHz framing rates at submicron spatial resolution and 64 pixels X 64 pixels per frame [7].

The shock loading device has exceeded our expectations in terms of ease of use, simplicity of installation in the SEM specimen chamber and the fact that its design has allowed us to bypass the development of a complicated shock-isolated stage. The subnanosecond pulse synchronization possible with the symmetrical version of this device is truly remarkable and may permit symmetrically-loaded dynamic experiments that otherwise could only be performed with expensive and less-well-synchronized laser or e-beam ablation loading. (The down-sides of our device of limited pressure peaks and material requirements are discussed above.)

We feel that this research effort has gone far to prove the feasibility of basic fast scanning electron microscopy concepts and the soundness of extrapolation of much of this technology to regimes of spatial and temporal resolution where important microstructural response research can be performed.

Figures 1 and 2 are photographs of the complete FSEM (fast scanning electron microscope) system as it exists at present.

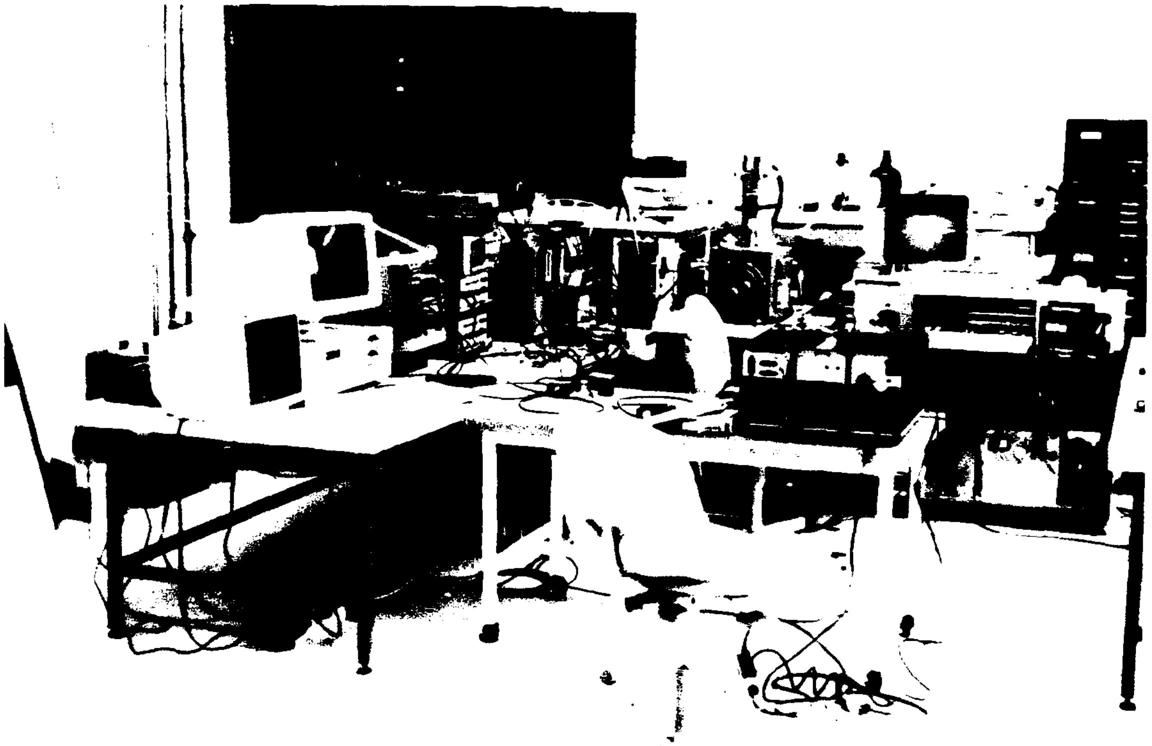

Figure 1. Oblique view of complete FSEM System.

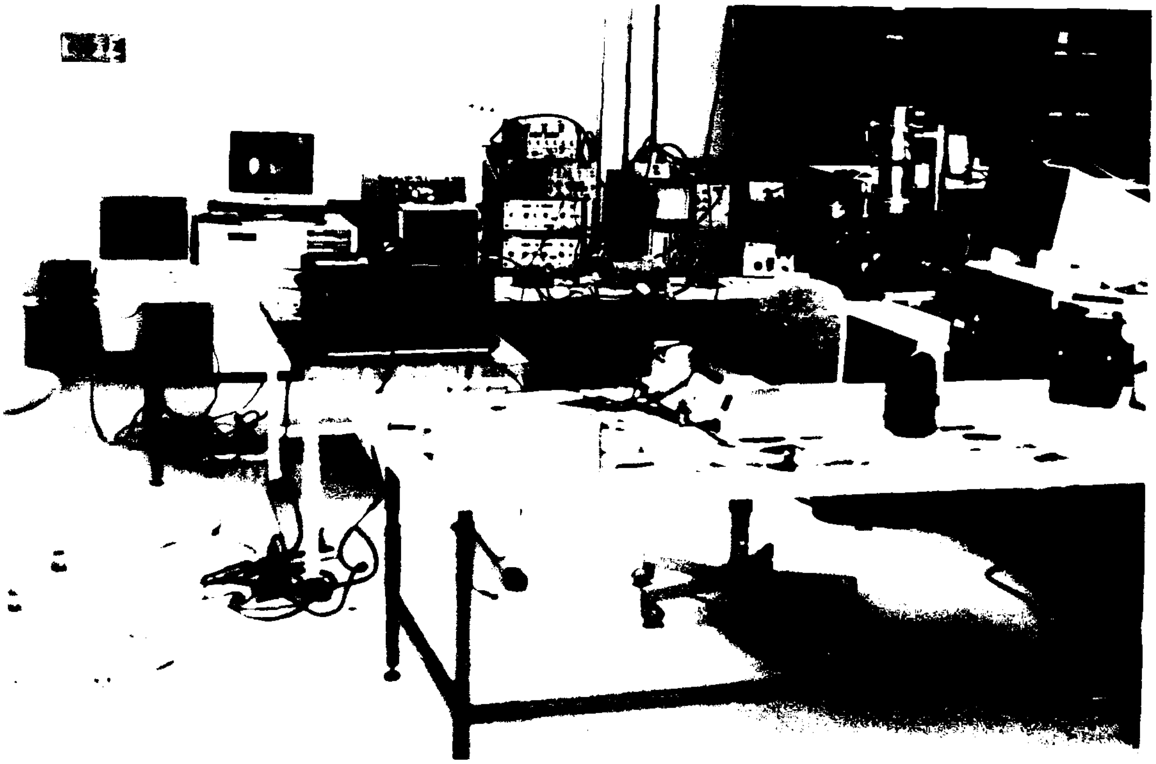

Figure 2. Frontal view of complete FSEM system.

II. Progress Since the Annual Report of 10/27/89

Since the Annual Report of 10/27/89, work has concentrated on three main areas: 1) improvements in system electronics, 2) development of the one microsecond pulse-width magnetically-induced stress wave device, and 3) first tests of the fast scan instrument in dynamic experiments.

1. Improvements in System Electronics

Several improvements to scan generator/scan coil driver electronics were performed. First, a problem arose due to the quiescent state of the scan generator producing a constant DC input to the scan coil drivers between scans. This resulted in image shift and unnecessary power dissipation in the scan coil drivers and scan coil termination resistors. This problem was fixed by placing a DC level shifter between scan generator outputs and the scan coil drivers.

Secondly, during tests to image 1/8" diameter rod specimens, lower magnification was required to properly center specimens in the microscope field of view. This was obtained by increasing the maximum current peaks output by the scan coil drivers by changing values of current limiting resistors in the op-amp circuitry.

Thirdly, at the higher deflection currents required for lower magnifications, significant heating occurs in the scan coil termination resistors. It was therefore decided to provide an option for adjusting magnification in easily-switched steps. With this modification, a low magnification image can be used for 30 seconds to position the specimen and then switched to higher magnification to prevent heat damage to the scan coil assembly.

Another modification which makes the microscope easier to use is a switch box permitting simple switching between analog data acquisition and digital data acquisition. The specimen is first positioned in the microscope field of view in analog mode, then switched to digital mode to take a digital movie.

Some time was also spent to synchronize fuse blow experiments with SEM scanning. In this case a charged capacitor was discharged through a 1 ohm resistor into Littlefuses of various current ratings. The current pulse through the capacitor was then used to start the scan generator. Some additional electronics was required to convert this pulse to a proper TTL pulse in order to start the scan generator.

Similarly, some time was spent to properly synchronize fracture obtained with the magnetically-induced stress wave device with the SEM scan. The pulse amplifier,driving the trigger generator which triggers the spark gap in the magnetically-induced stress wave circuit provides a precise timing signal for fracture experiments. Fracture occurs at a fairly well-defined time after this pulse is generated. The electronics developed for the fuse blow experiments was also used to convert the pulse amplifier sync out pulse to the proper TTL levels to start the scan generator.

2. Development of the One Microsecond Pulse-Width Magnetically-Induced Stress Wave Device

i) Electrical Calculations

Electrical calculations for the magnetically-induced stress wave circuit are given below, where we assume an underdamped series LRC circuit with constant L, R and C. Previous papers address other details of the concept such as geometrical dispersion, fracture localization and so forth [8-10].

As outlined in reference 10, we constructed an LRC circuit with a ~500 kHz resonant frequency. We used high-energy discharge capacitors capable of 25 kA peak current (four in parallel allows 100 kA peak pressure coil current) and 35 kV charge voltage. Capacitor inductance is nominally 60 nH (four in parallel reduces this value to 15 nH). Switch inductance is nominally <20 nH. The switch is able to handle 35 kA and 35 kV. A lower estimate for total system inductance without a pressure coil connected would be <35 nH. We exceeded this number by a factor of 5-6 as discussed below. However, this has not noticeably affected device operation.

In reference 10 we considered the possibility of using a hydrogen thyratron for a switch. However, we soon learned that for the currents and voltages of interest to us, pulse-widths of one microsecond were much too long for thyratrons. Further, thyratrons require considerable auxiliary circuitry. It was decided instead to use a gas-filled, mid-plane distortion spark-gap with UV illumination. UV illumination assures prompt turn-on and extends operating voltage down to the few kV charge voltages at which we expected to perform first tests.

Physically the circuit was built much as described in reference 10, although we used four capacitors instead of eight to test basic concepts. The four capacitor bank has served us well; increase to eight capacitors will double peak pressure and increase risetime by $\sqrt{2}$, all other items being equal. The basic pulse generator circuit is shown schematically below.

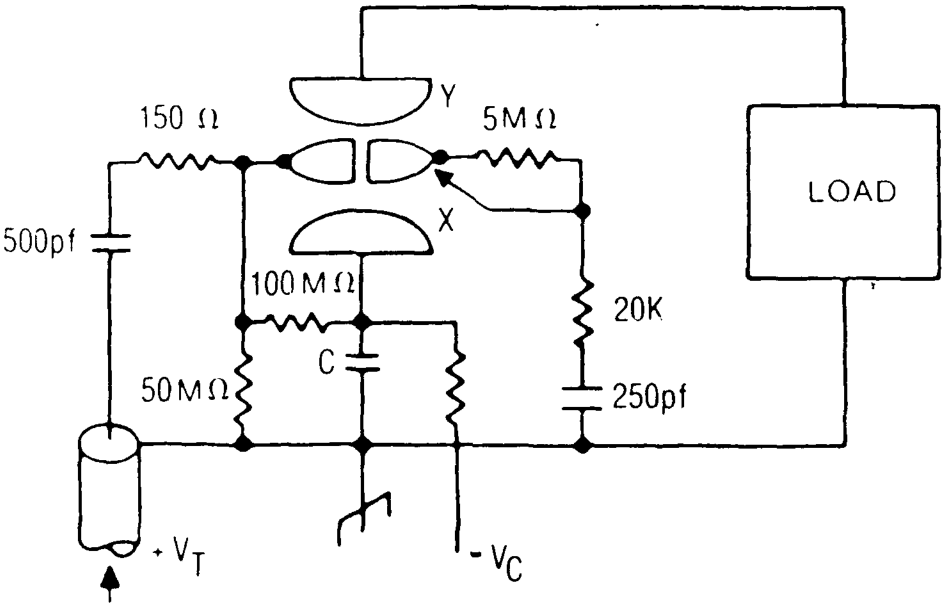

A simple analytic model for an underdamped series LRC circuit [9] is used in the analysis below.

Circuit variables are:

L--inductance
C--capacitance
R--resistance
Z_o--bank impedance
t--time
τ--resonant period
R_c--critical damping resistance
V_o--initial capacitor voltage
I(t)--current
I_{sc}--short-circuit current
I_{p1}--first current peak
I_{p2}--second current peak
t_{p1}--time of I_{p1}

Normalized circuit variables are:

$R' \equiv R/R_c$
$I' \equiv I/I_{sc}$
$t' \equiv t/\tau$
$I'(t') = e^{-2\pi R't'} \sin 2\pi t'$ (underdamped)

C is the given circuit variable. Quantities obtained from the measured current waveform are: t_{p1}, I_{p1} and I_{p2}.

Then we have:

$$R' = -1/\pi \ln |I_{p2}/I_{p1}|$$

(R' = 1 -> critically damped,
R'<<1 -> lightly underdamped)

$$\gamma = \tan^{-1} 1/R'$$

($\gamma = \pi/2$ for no damping)

$$\tau = 2\pi t_{pl}/\gamma$$

$$L = (\tau/2\pi)^2\ 1/C$$

$$Z_o = (L/C)^{1/2}$$

$$R_c = 2Z_o$$

$$I_{sc} = V_o/Z_o$$

$$R = R'R_c$$

$$I_{pl} = I_{sc}\ e^{-R'\gamma}\sin\gamma$$

We now have all quantities required to calculate the electrostatic energy, W_e, initially stored in the capacitor bank, the magnetostatic energy, W_m, stored in the pressure coil at current peak and the energy dissipated in circuit resistance. From these quantities we can derive efficiency expressions and estimates for peak magnetic pressure, p_m, generated by the pressure coil.

The main source of error in these calculations is probably the variable resistance of the switch. The gas-filled spark gap (Maxwell #40184) in the on state is a conducting plasma with time-dependent resistance (and, to some extent, time-dependent inductance as well). Also there is mutual inductance between the pressure coil and currents induced on the conducting rod. Computer simulations of the magneform process include such mutual inductances [11]; we feel mutual inductance effects are negligible in the present experiments.

Example Calculation

An example of a calculation of electrical parameters using the above expressions is as follows.

The capacitor bank for the one microsecond pulse-width device consists of four Maxwell #31687 capacitors in parallel. These capacitors have a total capacitance of 1.6860 X 10^{-7} fd (from calibrated values marked on the capacitors). The Rogowski coil/RC integrator current monitor was calibrated against a Pearson current monitor (Model 110A, factory calibrated to +1%, -0%) to give a sensitivity of 0.21333 V/kA. The bank short-circuit inductance was measured to be 163.4 nH. This is typically <10% of the total system inductance; most of the magnetic energy is stored in the pressure coil (and other places exterior to the capacitor bank, such as the transmission line and the interface at the SEM specimen chamber wall).

Figure 3 shows the circuit diagram for the measurement and a current waveform for TEST40 (floppy disk file name for digital movie) in which a 381 Hz framing rate SEM scan was synchronized with rosin fracture initiated within the SEM specimen chamber by free-end reflection of an incident compression pulse, resulting in fracture in tension, as indicated below in the Section on Probable Mechanism of Rosin Fracture at the Brass/Rosin Interface.

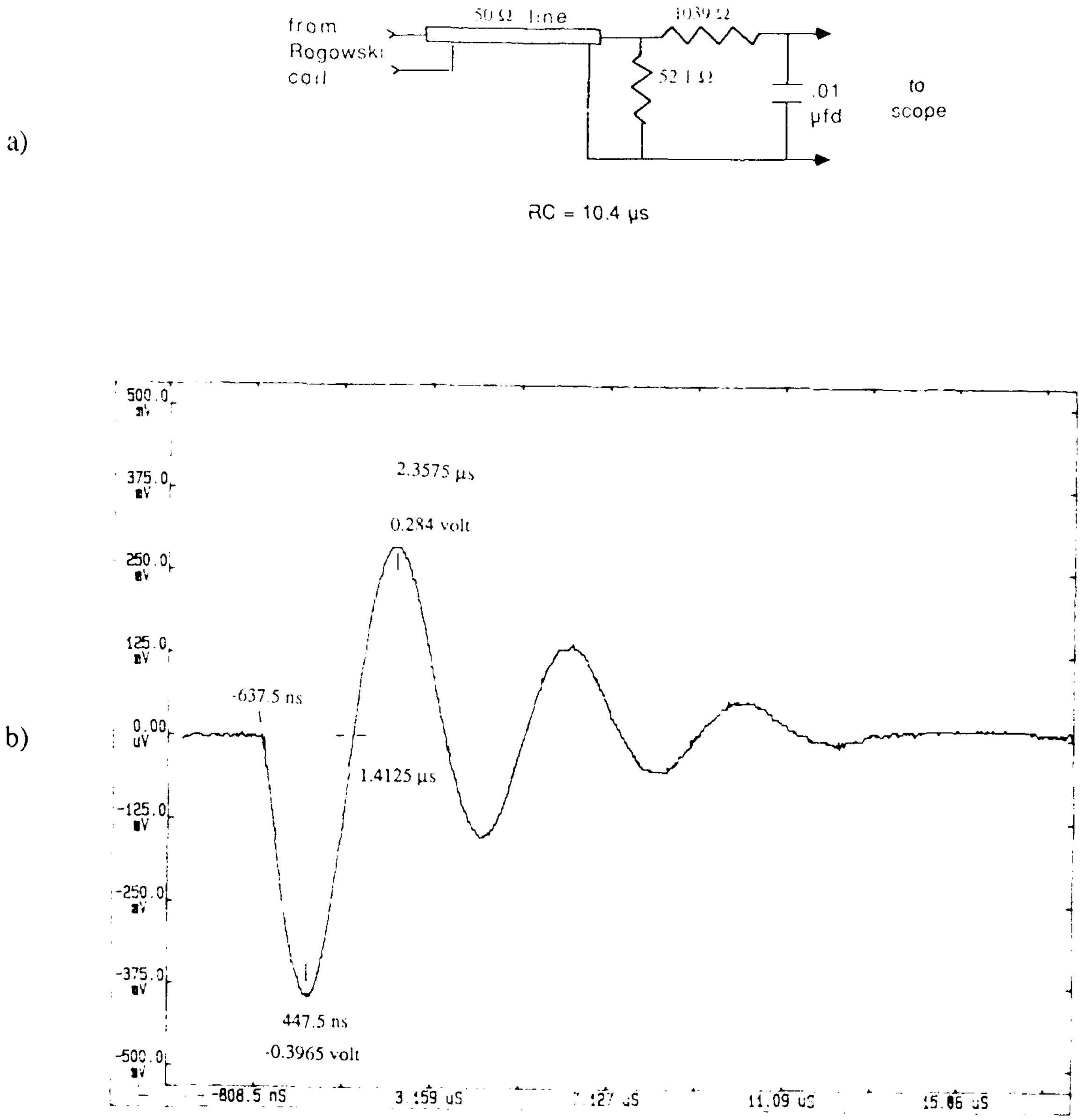

Figure 3. Measurement circuit diagram a) and current waveform b) for 381 Hz framing rate SEM scan of rosin fracture in tension.

Relevant electrical parameters for the version of the magnetically-induced stress wave device used in TEST40 are:

$I_{p2} = 1.324$ kA

$I_{p1} = 1.849$ kA (measured)

$t_{p1} = 1.085\ \mu s$

R' = 0.10622 (lightly underdamped)

$\gamma = 1.465$

$\tau = 4.653\ \mu s$

$L = 3.253\ \mu H$

$Z_o = 4.392\ \Omega$

$R_c = 8.785\ \Omega$

$R = 0.933\ \Omega$

$V_o = 10$ kV

$I_{sc} = 2.276$ kA

$I_{p1} = 1.936$ kA (calculated--within 5% of measured value)

$W_e = 8.43$ J

$W_m = 2.88$ J

$p_m = 1/3\ (W_m/\Delta V) = 4{,}434.3$ psi

Here ΔV is coil volume, $\pi \times 10^{-8}\ m^3$ (1 mm radius, 1 cm length). The 1/3 in the expression for p_m is discussed in reference 10.

We see that the conversion from W_e to W_m is not very efficient, ~34%. However even more inefficiency is desirable to produce more or less one pressure pulse with successive pressure pulses strongly damped out. Such a situation is shown in Figure 4. In terms of figuring out what's going on, a single pulse is far preferable; pulse amplitudes can be restored to higher levels to some extent by increasing initial capacitor voltage. However, at some point high-voltage breakdown at the pressure coil or elsewhere will require modifications such as coil potting or insulator convolutes.

Relevant electrical parameters for the current waveform shown in Figure 4 are:

$I_{p2} = 1.05$ kA

$I_{p1} = 2.98$ kA

$t_{p1} = 0.750\ \mu s$

$R' = 0.334$

$\gamma = 1.248$

$\tau = 3.775\ \mu s$

$L = 2.141\ \mu H$

$Z_o = 3.564\ \Omega$

$R_c = 7.127\ \Omega$

$R = 2.382\ \Omega$

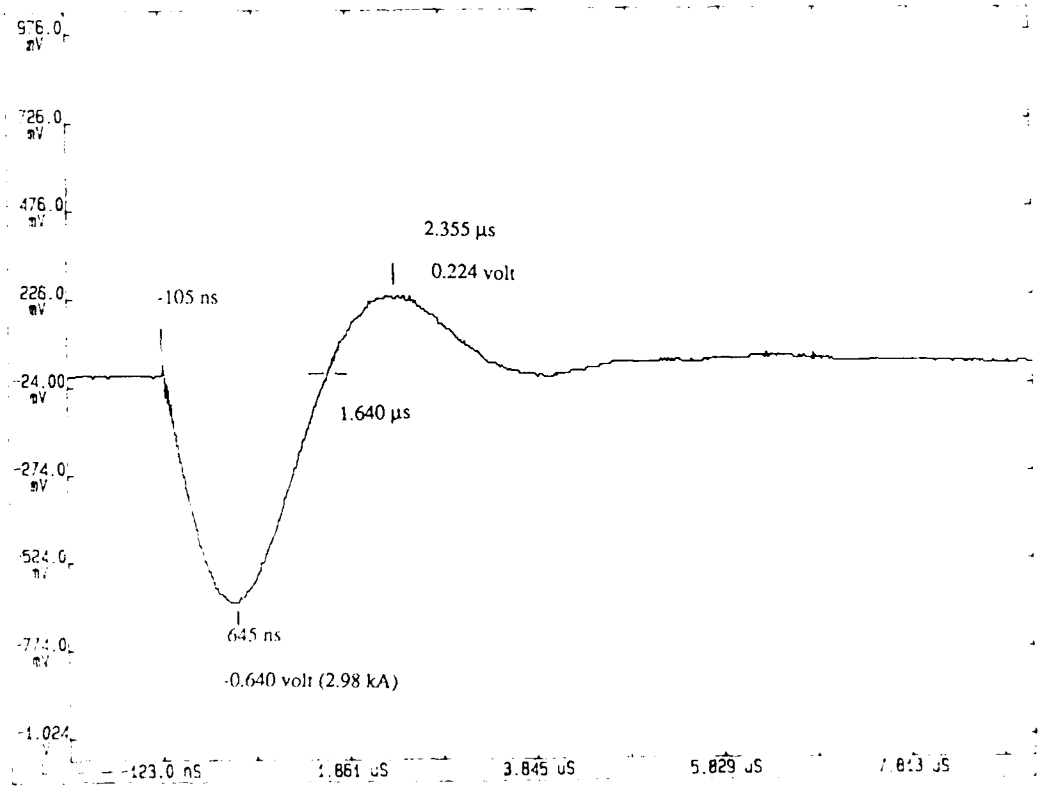

Figure 4. Resistive damping used to reduce current oscillations. Corresponds to magnetic pressure waveform shown in Figure 7 for piezoelectric plastic pressure measurement.

ii) Probable Mechanism of Rosin Fracture at the Brass/Rosin Interface

The first *in situ* fracture results with a simultaneous SEM scan were obtained with single-ended compression loading and fracture in free-end reflected tension with the compression pulse generated in a 1.03 mm radius brass rod attached to rosin rod of approximately the same diameter. At higher currents the rosin was found to fracture 1) in a two-thirds/one-third length fraction for rosin rod of ~2 cm length and a brass rod length of ~3 cm, and 2) at the brass/rosin interface. As circuit inductance increased as power cable length was increased and the high-voltage coaxial feedthrough at the SEM specimen chamber added inductance, the peak pressure was reduced, so that fracture only occured at the brass/rosin interface. However, it did so reliably and so was chosen for first *in situ* fracture scans.

Below we outline the mechanism we think is probably responsible for brass/rosin interface fracture.

variables:

ρ_i ~ mass density
E_i ~ elastic modulus
$c_i = (E_i/\rho_i)^{1/2}$ (thin rod pulse velocity)
$Z_i = c_i \rho_i$ (acoustic impedance)

Normalized Pressure Amplitudes

(For planar waves incident normally to interface
--slightly inappropriate to the actual situation.)

$$f = Z_1/Z_2$$

transmitted amplitude: $T = 2 Z_1/(Z_2+Z_1) = 2f(1+f)$

reflected amplitude: $R = (Z_2-Z_1)/(Z_2+Z_1) = (1-f)/(1+f)$

For $Z_1 >> Z_2$,

$T = 2$ and $R = -1$.

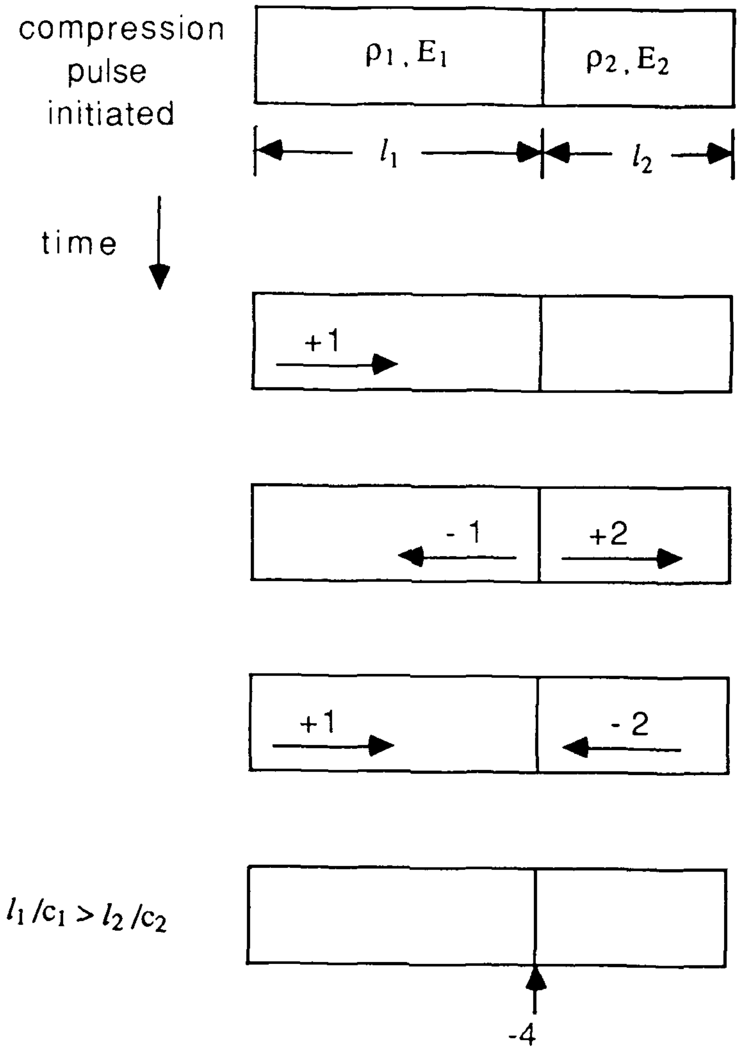

We see that for $Z_1 >> Z_2$ and $l_1/c_1 > l_2/c_2$, single-ended compression loading can result in ≤four-fold multiplication and inversion of the initial pulse at the material interface. Further details relating to geometrical dispersion, various modes of propagation and interface relations may be found in references 8 and 9.

iii) Ballistic Pendulum Peak Pressure Measurement

Due to our initial inability to fracture a variety of materials in rod form (1 mm rod radius), it was decided to make as direct a pressure measurement as possible by performing a ballistic pendulum experiment. (Materials we tried to fracture in tension produced by free-end reflection of single-ended compression pulses include: acrylic plastic, alcohol-embrittled acrylic plastic, borosilicate glass, scratched glass with water in the scratch, plaster of Paris, Portland cement, pencil lead, tile, solder and chalk.)

The ballistic pendulum was constructed by attaching a brass time-piece to nylon string and suspending it from the origin of a protractor. The compression pulse was communicated from a brass rod, subject to magnetic pressure, to the time-piece by the surface tension of a drop of ethanol. The coil was 1 cm in length, wound from #32 copper enamel wire and of diameter just slightly larger than that of the brass rod (nominally .081"). The movement of the time-piece was recorded with a VCR. The maximum height of the time piece was obtained from the length of nylon string and the maximum angle measured on the protractor. This maximum angle was fairly well determined because in one frame of the VCR tape where the angle was large, the time-piece was motionless, indicating zero velocity and maximum height.

The brass time-piece was measured to have a length of 5.588 mm, a mass of 0.1558 gm and a radius of 1.016 mm. Nominal values for brass are: thin rod pulse velocity of 3.32 mm/μs and mass density of 8.60 gm/cm^3. The pendulum mass rose to a maximum height of 8.0 mm, giving a kinetic energy of 1.221 X 10^{-5} J. The momentum was calculated to be 6.17 X 10^{-5} kgm-m/sec, with a maximum velocity of 40 m/sec. The capacitor charge voltage was 10 kV. The peak pressure coil current was 4.477 kA.

A first calculation assumed that the axially-directed impulse force was given by

$$F = F_o \sin^2 \omega t,$$

with impulse given by

$$P = mv = \int F dt = 1/2\, F_o\, \Delta t_1 \,,$$

where Δt_1 is the width of the first pressure pulse, measured to be 1.23 μs, giving a pulse length for the first pressure pulse of 4.08 mm. We soon realized that the time-piece was long enough to trap the momentum of the first two pressure peaks and perhaps <10% of the third (of greatly reduced amplitude) and that the second peak was not negligible, it was ~0.4 that of the first peak. This reduced our estimate of the first peak by 71.4%, giving a first pressure pulse peak of 3300 psi.

This calculation assumes $\sin^2 \omega t$ behavior for both pulses (with the above amplitude adjustment for each pulse). A more exact calculation would use the expression for $F(t')$ above, but experimental uncertainties do not justify such a careful calculation at present.

iv) Piezoelectric Plastic Pressure Measurements

Some effort was expended to try to measure pressure pulse amplitude and time behavior with piezoelectric plastic (Kynar®--a Pennwalt product [12]).

For these pressure measurements, we used a piece of Kynar 28 µm in thickness, with nominal sensitivity (d_{33}) of -33 pC/n. The mechanical response of this material is given by the time required for it to reach pressure equilibrium due to internal reflections, and is determined by material thickness over sound speed in the material. For this thickness of Kynar a response time of ≤20 ns has been cited.

As per instructions from Pennwalt people, we used low viscosity epoxy (RBC Industries, Warwick RI, #3215 resin with AB-503 hardener--100 to 75 by volume mix) to glue the Kynar between two pieces of 1/8" diameter brass rod. The plastic output was obtained in the charge mode ($V = Q/C$) giving a signal proportional to force (pressure).

Below is the circuit diagram for the measurement circuit. The capacitance of the transmission line is unknown although it is probably ≤100 pfd. Kynar has a nominal capacitance of 380 pfd/cm^2 and for a 1/16" radius specimen should have a capacitance of 30 pfd. There is some uncertainty in the transducer capacitance due to the thickness of the epoxy layers, but it should be small. The basic idea is that most of the piezoelectrically-generated voltage should appear across the 680 pfd capacitor.

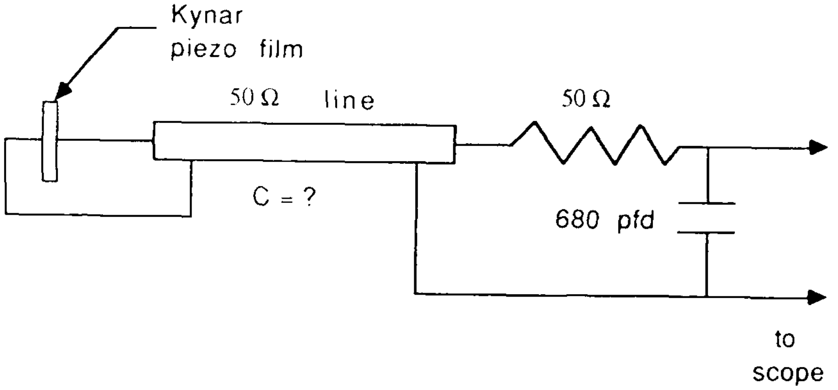

The first problem in making this measurement was to shield the plastic from the emp environment. The box shown in the photograph in Figure 5 and schematically in Figure 6 worked fairly well, as is seen in the waveforms of Figure 7. At early times there is noise on the transducer signal, but by the time the pressure pulse arrives at the plastic the results look plausible, although amplitudes are an order of magnitude low and there is much more going on than one would think by examining the magnetic pressure pulse.

The results are mystifying due to the low amplitude, the difference in FWHM between the input magnetic pressure pulse and the measured mechanical pulse, and numerous mechanical pressure pulses observed which cannot be due to reflections, given the lengths of rod indicated. It may be that positioning everything properly at such small dimensions requires extreme care. We may be exciting flexural modes due to non-axial alignment of the two brass rods, or radial compression of the pressure coil may produce unexpected modes. There are, of course, other ways to generate magnetic pressure. Moon used pancake coils [13], presumably to minimize radial compression, although the attenuation of B field from the plane of the pancake would mean going to much higher currents (hence higher voltages, presenting new electro-technical problems). At present we like solenoidal coils because they work so simply for double-ended tension pulse generation. (See next Section.)

Several other interesting experiments in this vein may also be worth pursuing. For example, using laser interferometry we may be able to extract pressure information by measuring rod free-end velocity. Also, it would be interesting to observe photo-elastic effects of a pulse propagating within, say, acrylic plastic rod. Photo-elastic studies could be performed with a fast framing camera or a time exposure with a strobed submicrosecond light source.

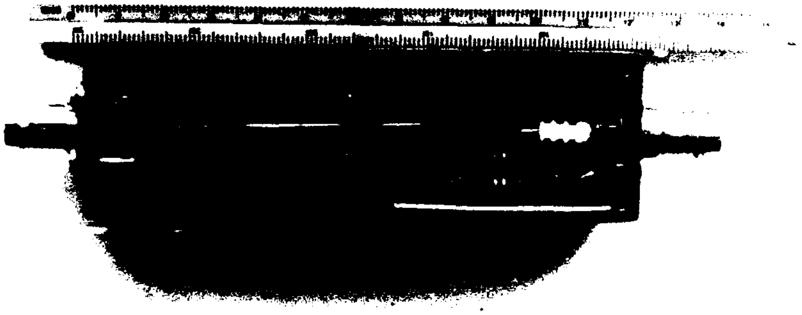

Figure 5. Photograph of box used to obtain shielded piezoelectric plastic pressure measurements of the magnetically-induced stress wave device.

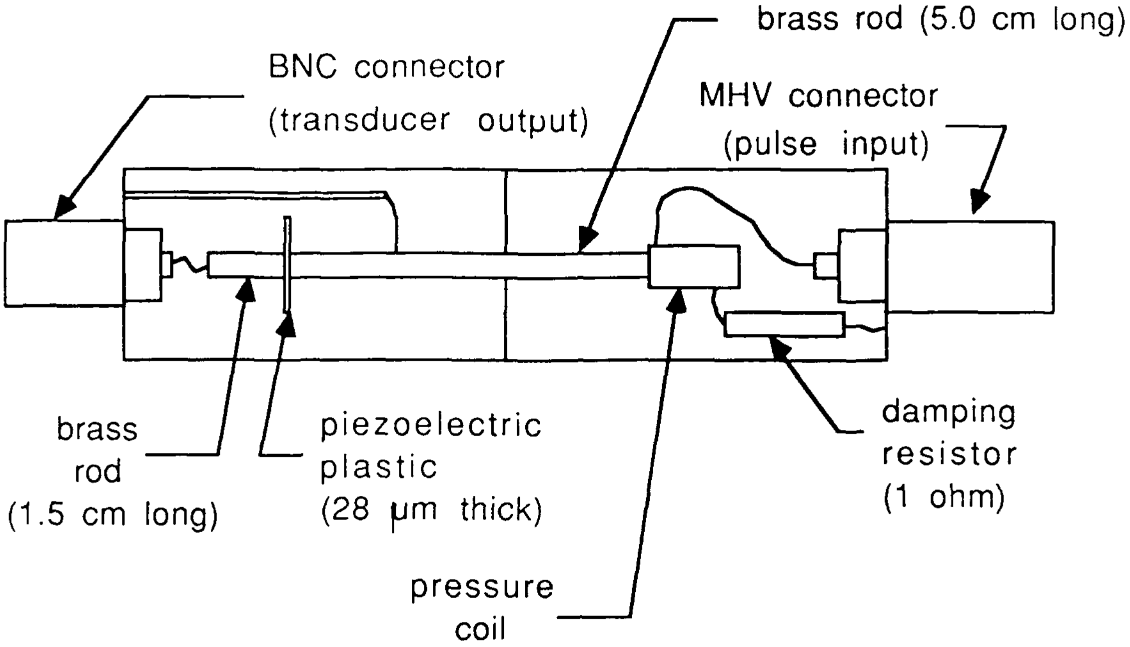

Figure 6. Diagram corresponding to Figure 5 indicating component placement within the box.

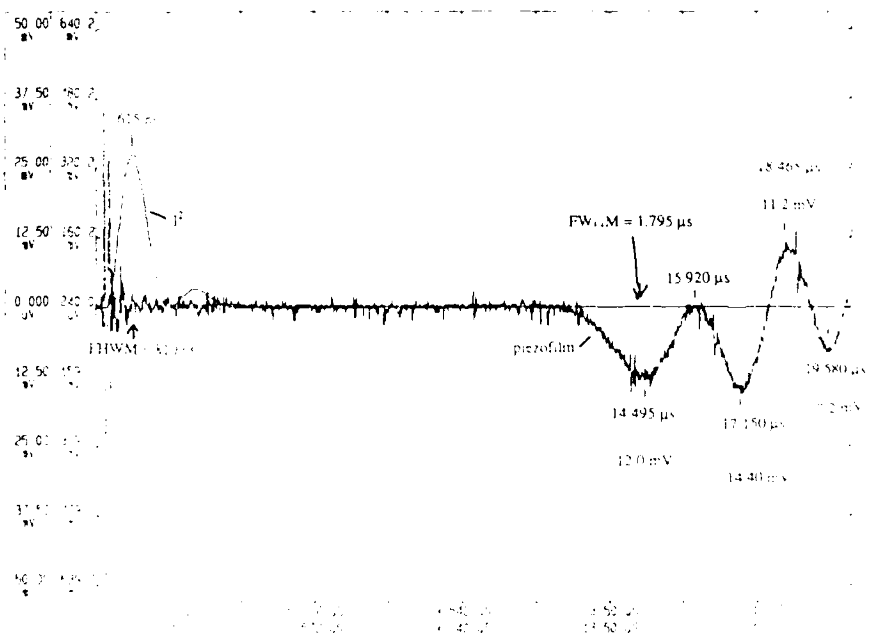

Figure 7. Waveforms of magnetic pressure and piezoelectric plastic output using the box shown in Figure 5.

v) Variations of the One Microsecond Pulse-Width Magnetically-Induced Stress Wave Device

Above we have discussed the probable mechanism of rosin fracture at the brass/rosin interface and mentioned rosin fracture within the bulk of the rosin sample which occurs at higher pressure coil currents with free-end reflection of single-ended compression pulse loading (resulting in fracture in tension). Below we discuss fracture within the bulk of the rosin, as well as double-ended tension (without free-end reflected pulse inversion).

Fracture within the bulk of the rosin probably occurs in two different places depending on whether the pressure current waveform is lightly damped or heavily damped. For example, for a completely undamped waveform, at some time the first compression pulse will have undergone reflection (and free-end reflected inversion) and will overlap the second compression pulse, resulting in no net pressure at that time over one pulse length. This situation is shown in Figure 8 f. Earlier in time (Figure 8 d), the last half of the first compression pulse cancels the inverted first half of the first compression pulse.
By Figure 8 g, the reflected first pulse has attained full amplitude and fracture will occur at that time (or slightly before if the first pulse peak amplitude exceeds the pressure threshold for fracture). Realistically, current waveforms are always damped to some degree and when such effects occur, the sum of the inverted first pulse and non-inverted second pulse will result in a small tension pulse at times corresponding to Figure 8 d and 8 f.

If the current waveform is damped enough that the second pressure pulse and subsequent pulses are negligible compared to the first pulse, we will have situation like that shown in Figure 9. Note that in Figure 9 f the last half of the compression pulse is canceled by the first half of the reflection tension pulse. Such a situation can only occur, of course, if the pressure pulse is perfectly symmetrical, which is seldom the case.

The most realistic pressure pulse waveforms are given in Figures 10 and 11. These Figures assume $(e^{-2\pi R't'} \sin 2\pi t')^2$ pressure dependence for the first three half-resonant periods. In Figure 10, R'=0.10622, corresponding to the current waveform shown in Figure 3. In Figure 11, R'=0.334, corresponding to the current waveform shown in Figure 4.

Unfortunately, as discussed previously, to obtain a damped waveform at fixed charged voltage reduces the amplitude of the first pressure peak (and decreases its risetime) so that a direct comparison between fracture points in the lightly damped and damped situations at the same charge voltage is not possible. (These changes in waveform are evident in Figures 10 and 11, where waveform amplitudes are normalized to the R'=0 value.) Even for a rough comparison it may be necessary to increase capacitor bank charge voltage to levels where "electrotechnical" problems such as high-voltage breakdown become serious.

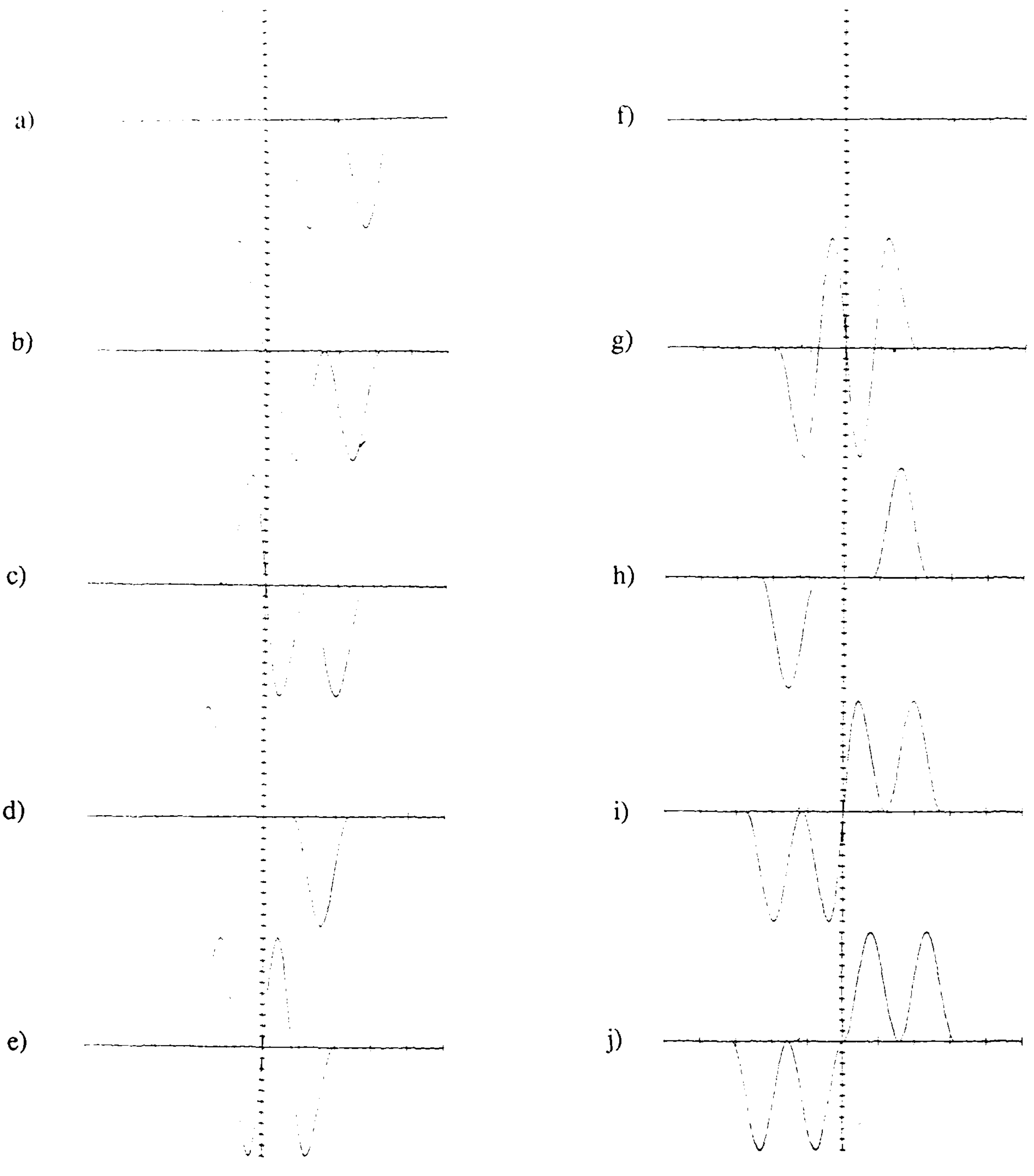

Figure 8. Free-end reflection of an undamped double-pulse train with $p \propto \sin^2 \omega t$.

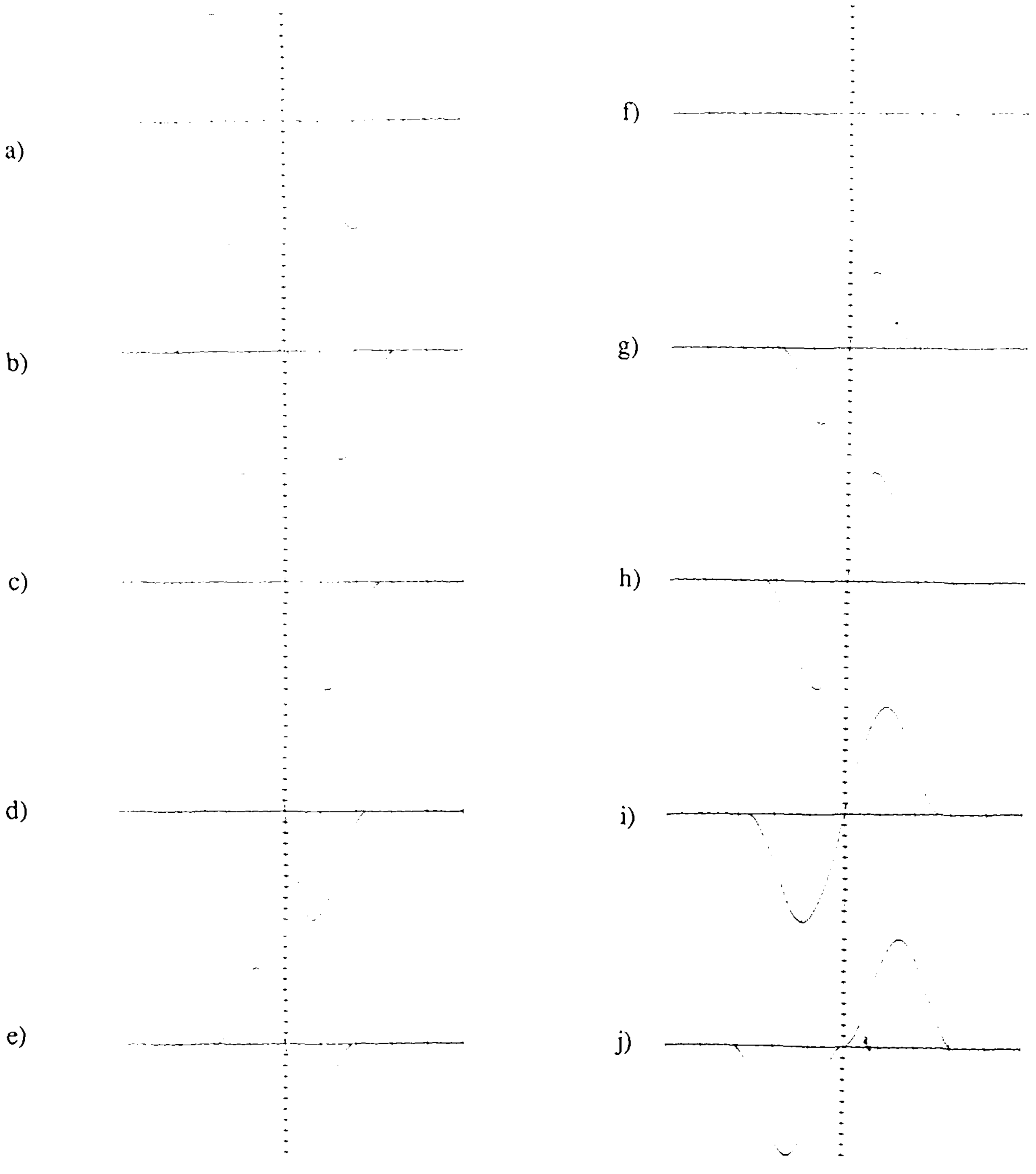

Figure 9. Free-end reflection of a single undamped pulse with $p \propto \sin^2\omega t$.

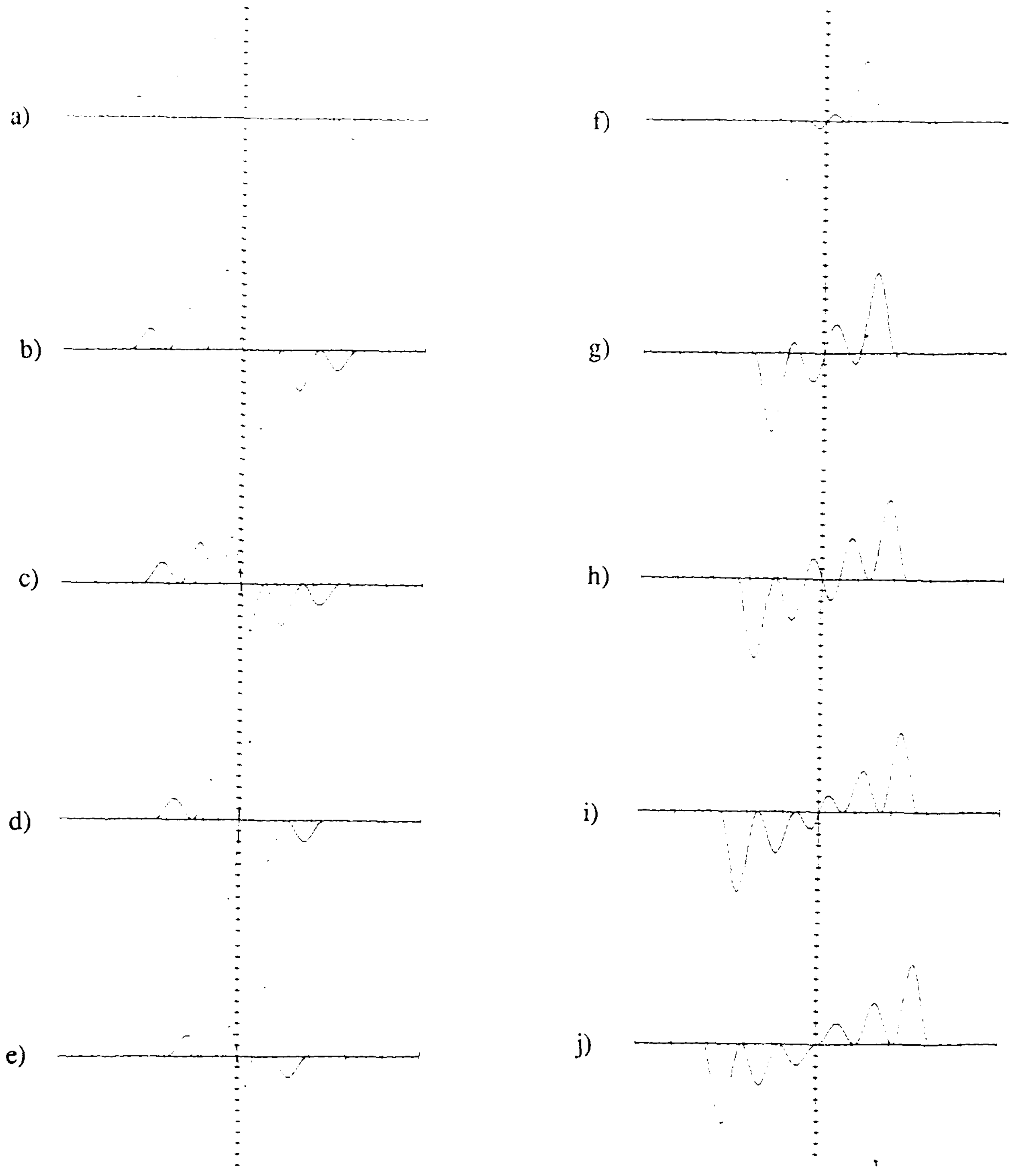

Figure 10. Free-end reflection for the first three half resonant periods of a pressure pulse train with $p = (e^{-2\pi R't'} \sin 2\pi t')^2$ and $R' = 0.10622$, corresponding to the current waveform shown in Figure 3.

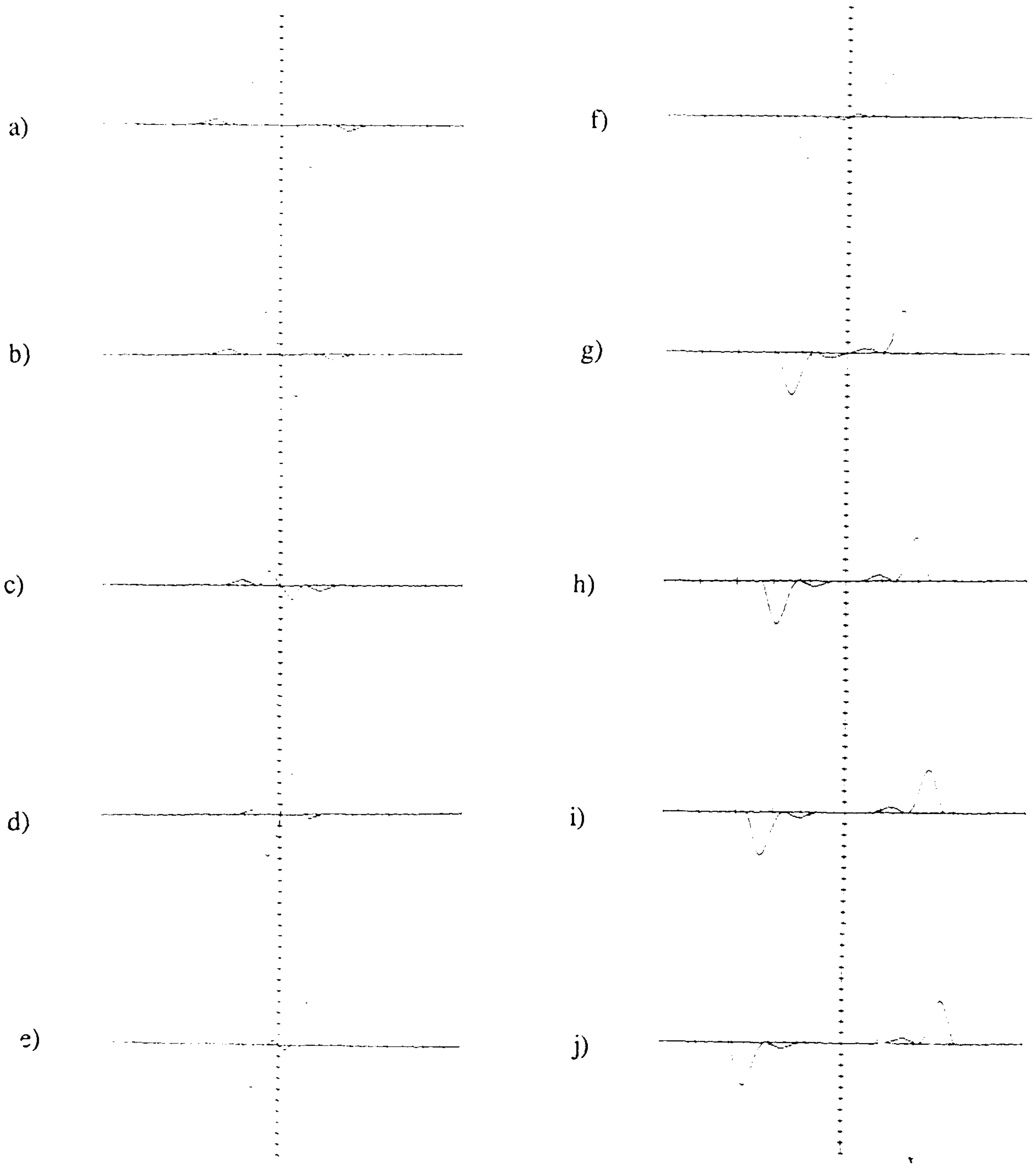

Figure 11. Free-end reflection for the first three half resonant periods of a pressure pulse train with $p = (e^{-2\pi R't'} \sin 2\pi t')^2$ and $R' = 0.334$, corresponding to the current waveform shown in Figure 4.

The double-ended tension concept has proven to be remarkably simple to implement. Originally we believed it would be necessary to build two separate pulse generators and to synchronize them with a single high-amplitude, fast trigger pulse. However, as it became clear that these experiments required specimens typically 1-5 cm in length, we realized that all we had to do was put two coils in series. Then coil separation is typically under 10 cm or so and pulse synchronization is approximately within that distance divided by light speed, which means subnanosecond synchronization. Then uncertainty in fracture location will be determined as indicated in references 8-10. The basic concept is shown below.

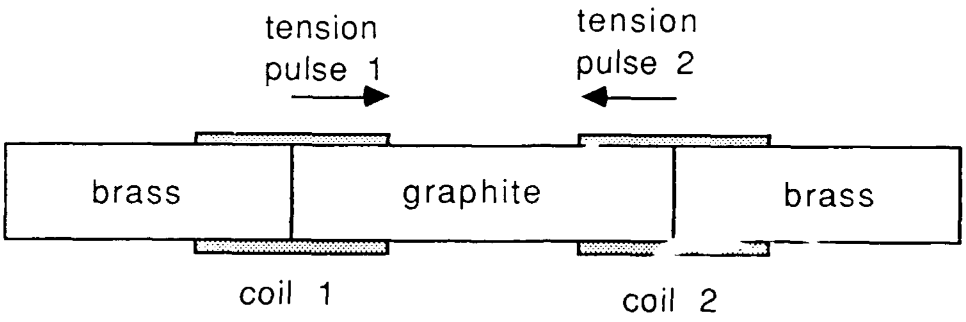

Double-ended tension is particularly simple for specimens that are non-(electrical) conductors, such as rosin. The concept was first tested with graphite, however, which is merely a poor conductor. In fact the skin depth in carbon for 500 kHz (resonant frequency for one microsecond pulse-width) is comparable to 1 mm, the typical rod radius of these experiments [10]. The first test of double-ended tension with graphite is shown schematically below. It did not result in fracture probably because the graphite used was in fact pencil lead which has clay in it and other impurities. (We have since obtained pure samples of polycrystalline graphite from Poco Graphite which have nominal static tensile strengths of 3,000 psi.) We are convinced that tension pulses were in fact generated due to observed reaction impulses on the two pressure coils towards the center of the graphite rod.

3. First Tests of the Fast Scan Instrument in Dynamic Experiments

i) Bead Blast Beads

To demonstrate the dynamic capabilities of the instrument, we placed some bead blast beads, small glass spheres used to clean and finish materials in a sandblast-like process, onto a piezoelectric transducer. The transducer was excited by a waveform to cause the spheres to move rapidly enough to provide an interesting digital movie at 381 Hz framing rate. We believe the movie demonstrates the soundness of our approach to dynamic microscopy.

To increase S/N, the final SEM column aperture was increased to a minimum of 1 mm. This reduces depth of focus; a brighter source would allow for comparable S/N but increased depth of focus, hence increased image sharpness.

This movie was put into a VCR format and copies of it were sent to AFOSR and to a number of interested parties.

ii) Fuse Blow

Our next experiment was to attempt to image the opening of a small fuse. After experimenting with such fuses we found that they could be made to open in tens of milliseconds after applying a high-current pulse to them. At 381 Hz, the time per frame is 2.62 ms; we initially hoped such an event could provide an interesting movie.

We encountered some unexpected problems, however. After applying the current pulse, the image quality would decrease dramatically. A few frames later the fuse would re-appear. Then the image would be washed out completely for several frames. After washout the fuse would be visible again. We believe that what happens is that after current is applied, the fuse heats up enough to outgas absorbed gases but not enough to melt and open. Outgassing means that near the fuse the primary beam electrons may be scattered somewhat and secondaries may be scattered so much that image quality is greatly degraded. We believe the image re-appears after outgassing ends. We believe the second wash-out was caused by the fuse wire heating to incandescence, whose light swamps the PMT.

To prove this we spent some time improving the light-shielding around the PMT and around the fuse. This essentially eliminated the second washout problem.

We also speculated that when the fuse is heated to incandescence it becomes a thermionic electron source that swamps the secondary electron signal. To test this idea, we took a two-volt incandescent bulb and removed the glass envelope. The bulb was then placed inside the specimen chamber where the fuse had been and current passed through sufficient to make the filament glow brightly. This was with light shielding of the PMT and filament in place. The image of the filament on the CRT screen was not affected in these experiments, thus the thermionic contribution is believed to be negligible.

After eliminating the light problem, we found that though the fuse takes tens of milliseconds to open, the visual process of the fuse opening takes less than 2.62 ms. That is, with the present limited image sharpness available with our tungsten cathode, we see no evidence of melting or other changes in the fuse surface until from one frame to the next, a small section of fuse disappears.

Figure 12 shows four frames from a digital movie taken with light-shielding around the PMT. Figure 12 a is the fuse wire after current has been applied but before anything interesting happens to the fuse wire. Figure 12 b shows what we believe to be the effects of outgassing on the image. Though image quality is poor in this frame, it seems adequate in the vicinity of where the fuse wire later opens to say that at this time the wire has not yet opened. However, in the next frame shown in Figure 12 c, 2.62 ms later, the wire is open. Figure 12 d is a better quality image of the open fuse taken after the outgassing problem has disappeared.

Microscope operating parameters for the data shown in Figure 12 are as follows. Beam voltage--3 kV. Working distance--65 mm. Tilt--0°. No final aperture (≥1 mm diameter). Specimen current--55 nA (Maximum spot size). Pixel rate--25 MHz. PMT voltage-- -1300 volts. Everhart-Thornley collection bias-- +200 volts.

At this pixel rate there were ~13750 primary electrons/pixel (assuming specimen current ~ probe current). Assuming $f\,\delta = 0.1$, S/N ~ 37, where f is detector collection and detection efficiency and $\delta(V)$ is specimen secondary electron yield. (S/N, of course, is drastically reduced during frames 12 b and 12 c when f is drastically reduced by secondary scattering through outgassing gases.)

The primary beam semi-convergence angle is ≥ 7.69 mrad.

Figure 12 a. Frame 1 of fuse blow movie. Data disk filename--A7. Data taken 5/23/90, 2:34 pm.

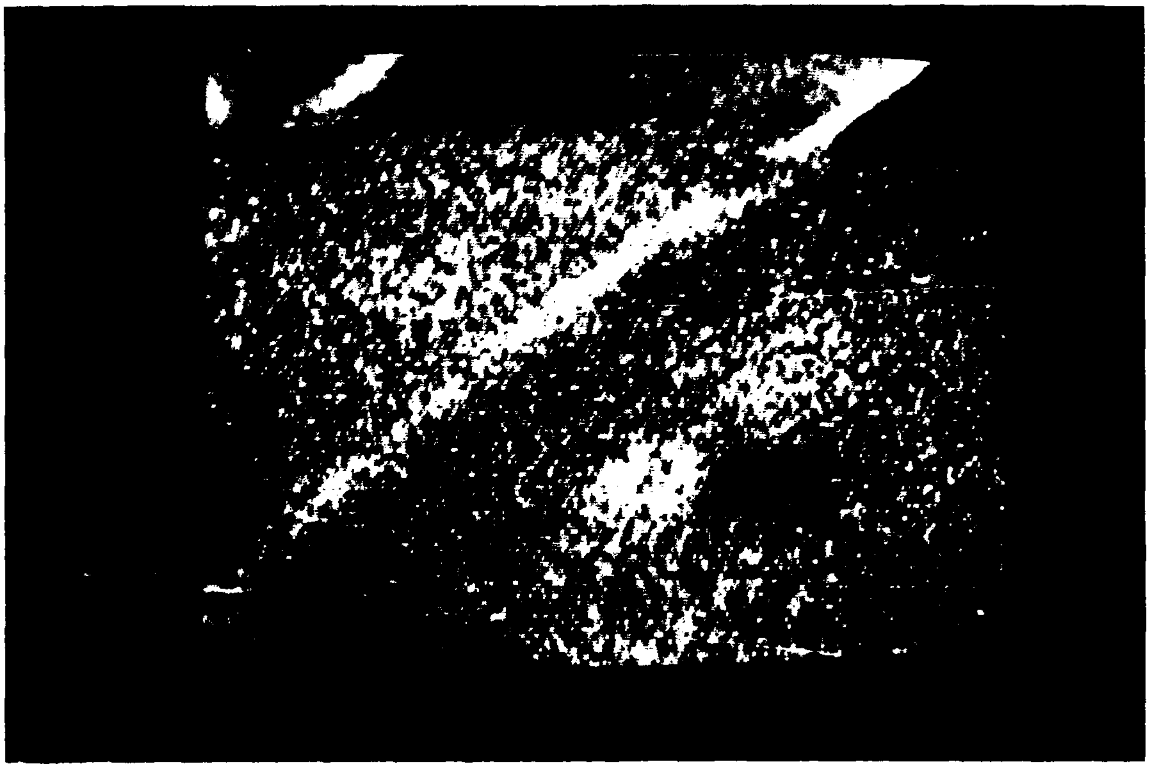

Figure 12 b. Frame 3 of A7 data. Note washout problem (probably outgassing) in lower part of frame. (This frame was scanned top to bottom.)

Figure 12 c. Frame 4 of A7 data. Note that fuse wire is already open.

Figure 12 d. Frame 6 of A7 data.

iii) *In Situ* Dynamically-Loaded Fracture

Once we demonstrated that rosin could be fractured in tension with the single-ended compression version of the magnetically-induced stress wave device, we wanted to attempt to image fracture dynamically using this fracture method.

The first concern was that the emp generated by the magnetically-induced stress wave device might damage the electronics in the data acquisition system, the detector system or in the SEM itself. Our second concern was that even if no electronics were damaged, it might take too much time for the electronics to recover from the emp to obtain a decent scan.

Our original concept was to place the magnetically-induced stress wave device capacitor bank and switch in an electromagnetically shielded box constructed from copper or brass screen or sheet. We also planned to similarly shield the Patco pulse generator, which produces a ~50 kV amplitude pulse in a few nanoseconds. (This pulse generator is notoriously noisy mainly because its output pulse is seldom terminated in order to get maximum pulse amplitude and minimum pulse risetime for good triggering.) However, we soon decided to place both these components, plus the capacitor bank charge supply and associated equipment entirely in the double-shielded electromagnetic enclosure used in earlier experiments with the 75 μs magnetically-induced stress wave device. Feedthroughs were then provided for spark gap switch gas flow, capacitor bank voltage monitor, pulse trigger input, pulse trigger sync out, pressure coil current monitor and a coaxial transmission line feed from the capacitor bank to the pressure coil.

This set-up worked well in initial tests in which a ~2 ft length of RG59 cable connected from the double-shielded enclosure to a small Pomona box with an MHV feedthrough and the pressure coil, as shown in the photograph of Figure 13 and schematically in Figure 14. Figures 15 and 16 show the box mounted on the specimen stage for the digital movie frames shown in Figures 17. Rosin was reliably fractured at 10 kV charge with this set-up. It fractures at the brass/rosin interface and in the "two-thirds/one-third" manner described above. The probable mechanism for the later fracture mode is described above for two situations. The first situation is the case where the current waveform is lightly damped, leading to a succession of pressure pulses. The second situation is the case where essentially one pressure pulse is generated.

Figure 17 shows two frames from two digital movies. Figure 17 a shows the brass/rosin interface before application of the pressure pulse. In this case only interface fracture was observed. The brass rod is at the top of the frame, the rosin at the bottom. Figure 17 b shows the interface after application of the pressure pulse. In Figure 17 b the rosin is completely gone from frame and the break is fairly straight.

Microscope operating parameters for the data shown in Figure 17 are as follows. Beam voltage--1 kV. Working distance--66 mm. Tilt--+0.50°. No final aperture. PMT voltage-- -1490 volts. Everhart-Thornley collection bias-- +200 volts. The primary beam semi-convergence angle was ≥7.58 mrad.

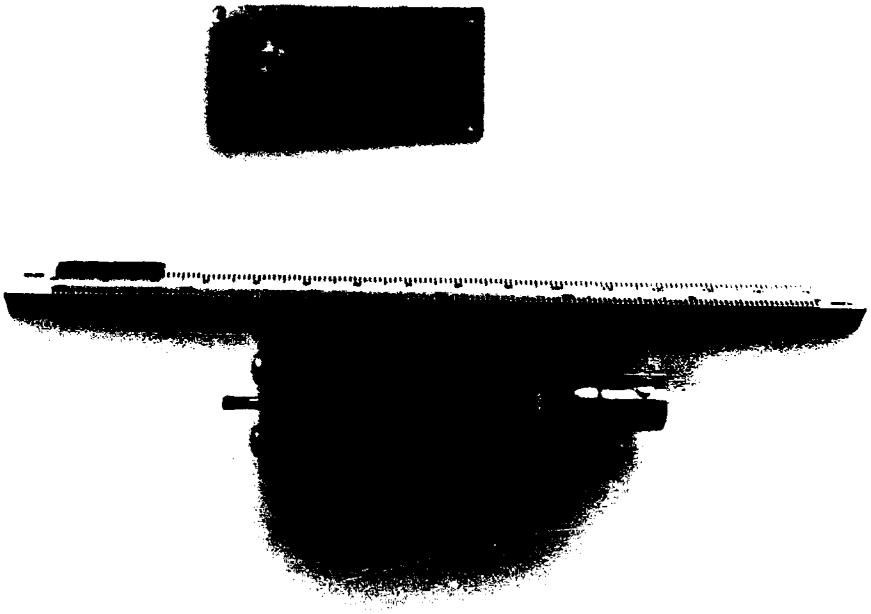

Figure 13. Top view of the box used to obtain *in situ* rosin fracture in tension. The piece of rosin resulting from fracture at the brass/rosin interface is shown on the centimeter scale.

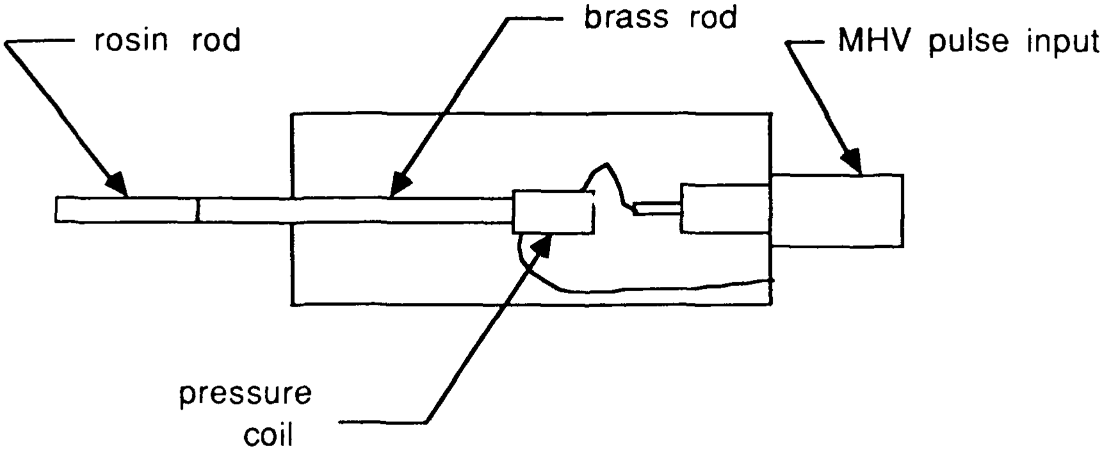

Figure 14. Schematic diagram of the box shown in Figure 13 identifying main components.

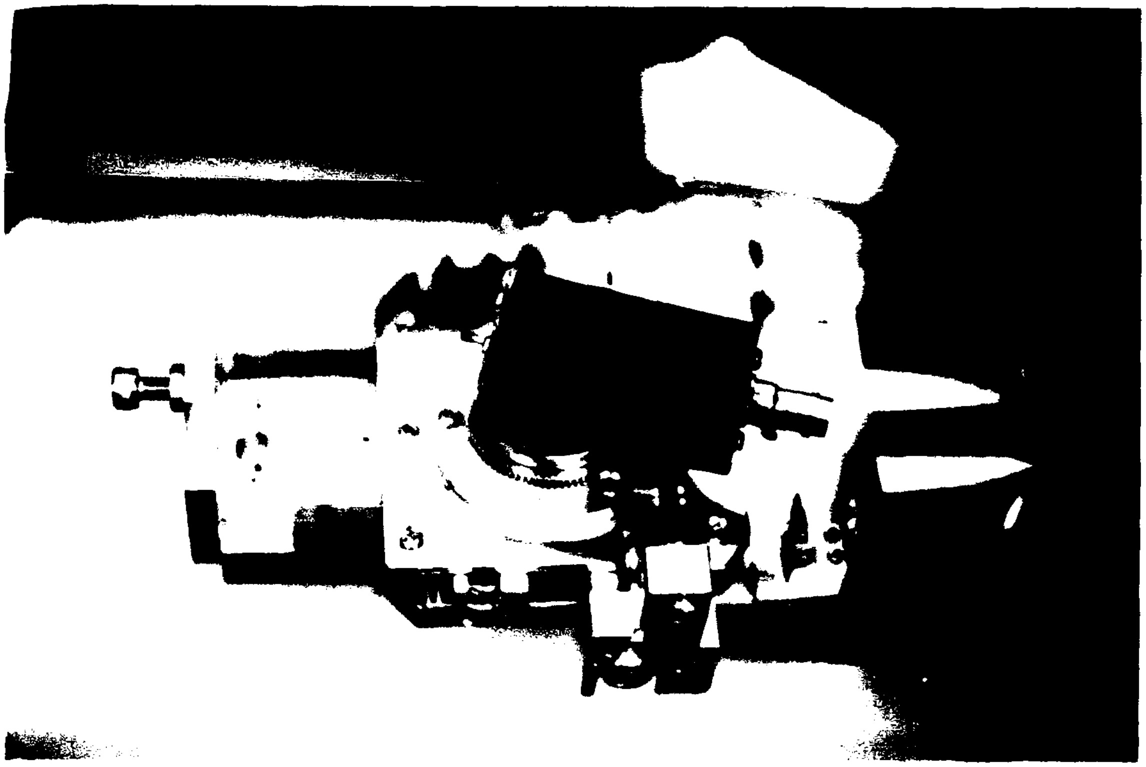

Figure 15. Photograph of box of Figure 13 mounted on the SEM specimen stage.

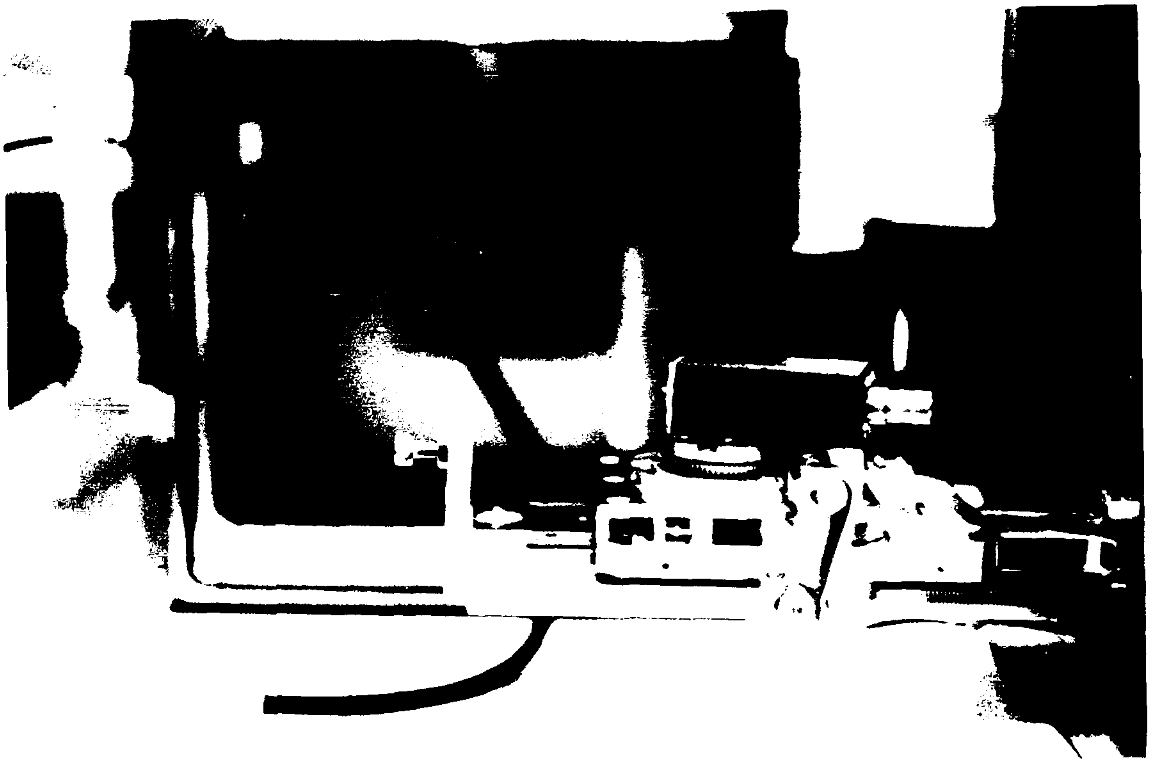

Figure 16. Photograph of box of Figure 13 after a successful fracture test within the SEM chamber. Power feed cable is shown disconnected.

Figure 17 a. Frame from TEST39 showing the brass/rosin interface before application of the pressure pulse. Brass is at the top, rosin at the bottom. The rod is 1/8" in diameter.

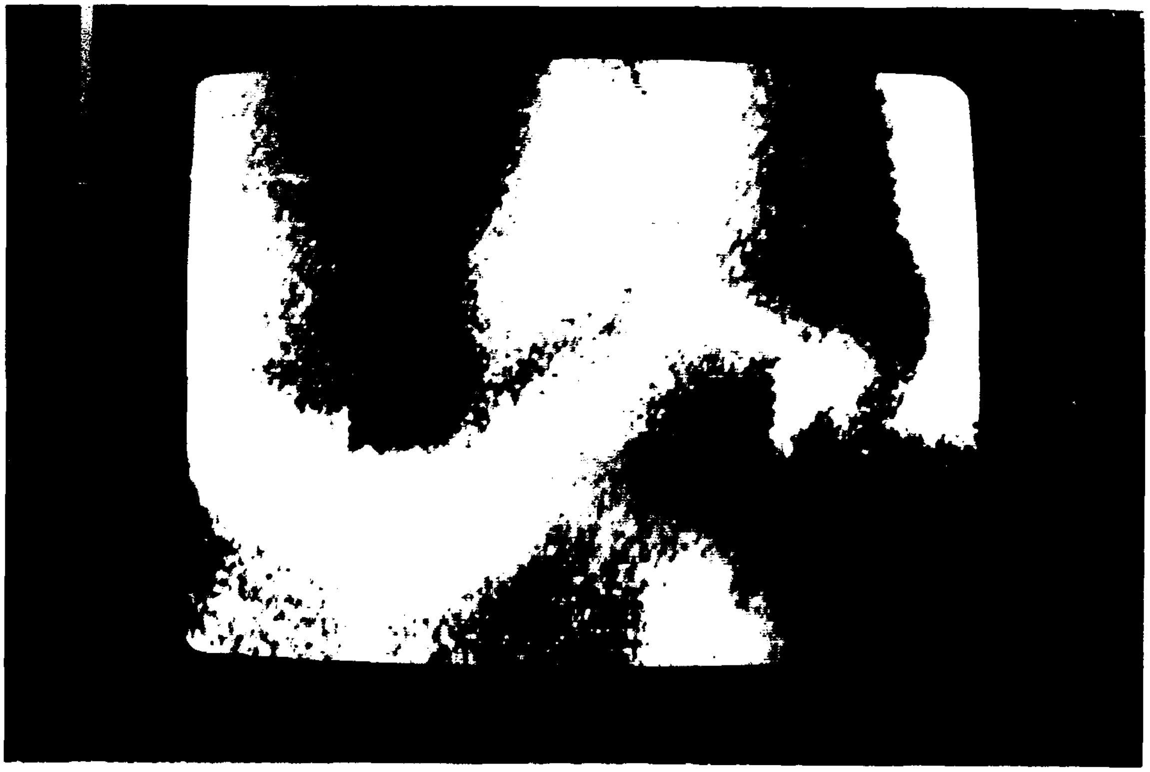

Figure 17 b. Frame from TEST40 showing brass/rosin interface after application of the pressure pulse.

iv) Integrated Circuit Inspection

In our effort to find possible applications for the fast scan microscope, our consultant, Dr. Mackinnon, suggested that high-speed inspection might be of interest. One inspection application he mentioned was that of integrated circuits.

We spent some time exploring this issue because we initially believed it was a possible way to obtain the higher brightness cathode we need to do advanced fracture experiments.

We contacted several people at SEMATECH in Austin, TX, a consortium of U.S. chip manufacturers whose operating budget is shared jointly by consortium members and DARPA. We contacted Dr. Sudhakar Kudva, who oversees SEM operation at SEMATECH. After discussions with people recommended to us by Dr. Kudva (initially people at Amray and at Ångstrom Measurements), a white paper was written in preparation for a presentation to SEMATECH on April 19, 1990.

In the course of preparation for this presentation and as a result of discussions resulting from the presentation, we learned that multiple secondary electron detectors are used in the Ångstrom Measurement machines to obtain a balanced image and to increase detector current to increase S/N. This technique had been proposed earlier for our project by Bob Macy. It was reassuring to see it used successfully in an advanced critical dimension measurement SEM. We also learned that the requirements for this sort of inspection are rather stringent: beam voltages ≤1 kV are required to reduce specimen charging and chip damage; spatial resolution in the 10-100 Å range is required; image linearity and stability are paramount; pixel resolution of ≥512 in each direction is preferred. It was soon determined that we could not meet these requirements very easily.

III. Comparison of Statement of Work with Research Performed

a. *reconfigure an SEM to accommodate the proposed modularity concept.*

The modularity concept was used to reconfigure an SEM, the ISI SX-40A. The deflection coils and their drivers were replaced with higher bandwidth components. The detection system was also replaced with a higher bandwidth system. The data acquisition system was replaced with a fast digital data acquisition system. The specimen chamber was modified to permit an electrical feed-through to the pressure coil assembly.

b. *continue developing the symmetrical magnetic impulse loading device designed and initially tested in Phase I. (1 microsecond system with peak pressure to 10,000 psi).*

The magnetic impulse device was built and tested in a single-ended compression version with a ballistic pendulum to a peak pressure of 3300 psi with a pulse-width of 1.23 µs at a capacitor charge voltage of 10 kV. This version of the device was tested to a capacitor charge voltage of 20 kV, corresponding to a peak pressure of 13,200 psi.

The device was also configured to obtain symmetrically-loaded tension at comparable pressures and pulse-widths.

c. *complete the design and fabrication of the isolation and protection device for the SEM.*

The design for shock isolation was considerably simplified by miniaturizing the loading device, allowing pulse generation entirely within the SEM specimen chamber, requiring no mechanical feed-through isolation. The reaction pressure pulse is effectively absorbed by wires holding the pressure coil in place.

As mentioned in the Annual Report [2], it was decided that the problem of specimen dust ejecta entering the SEM column was less important than originally believed due to the small solid angle subtended by the final aperture from the specimen. Further, the SEM column liner is easily removed should any cleaning be required.

d. *design and build a digital acquisition system with the capabilities as described in the proposal. (500-750 MHz, 1000 frames of 100 X 100 pixel data, etc.)*

A digital data acquisition system was assembled to provide scan signals synchronous with data acquisition. The data acquisition system itself is capable of 200 MHz pixel rate with total storage of 1 Mbyte which, for 256 pixels X 256 pixels per frame, allows for total storage of 16 frames. This storage capability can easily be expanded to 32 frames with additional memory modules.

The limiting factor in pixel rate has been primarily the signal-to-noise ratio available with the tungsten hairpin cathode we have been working with. We have obtained useable images at 25 MHz pixel rate. A second limitation has been the scan generation circuitry, limited to 25 MHz pixel rate at present. We have obtained analog acquired signals at an effective pixel rate of >50 MHz which is probably close to the limit for the secondary electron detector we have developed.

e. *complete the study of increasing the scan rate to the maximum obtainable with existing deflection coils.*

It was soon determined (May 1989) that the existing scan coil assembly and drivers introduced severe image distortion at even the slowest framing rate (47.4 Hz at 256 pixels X 256 pixels), so efforts quickly focused on developing faster scan coils and drivers.

We have used our fast deflection coils and drivers down to 1.6 μs horizontal line time and routinely operate at 10.25 μs horizontal line time. For comparison, TV-rate horizontal line time is typically 60 μs. A 1.6 μs horizontal line time means a framing rate of >1 kHz would be possible at 256 pixels X 256 pixels if the scan generator could operate at higher pixel rates (presently limited to 25 MHz).

f. *complete the development of impulse device and specimen field of view.*

The impulse device was completed in a form which permitted *in situ* fracture of a weak brittle specimen within the field of view of the microscope with fracture timed to occur with scanning.

g. *complete the development of increasing the scanning and recording rates.*

Having attained the values listed in d. above, it was clear that useful imaging at higher rates could only be obtained with a brighter cathode. Several efforts were made to obtain such a cathode but to date we have not been able to obtain one.

However, in anticipation of obtaining such a cathode, designs were completed for scan coils and drivers able to take us to 200 MHz pixel rates, partly because of the cost of the preferred Zr/W gun (~$60,000).

h. *optimize the system (including magnification and resolution requirements.)*

For any given experiment the beam voltage, deflection current, beam spot size, specimen working distance, detector placement and bias were adjusted to give the best digitized image. In general it was found necessary to increase final aperture diameter to obtain good signal-to-noise ratio in the final image. This necessarily reduced the depth of focus in the image, restricting that portion of the field which is well-focused. Lower magnifications were desirable from a standpoint of understanding what was occuring in an *in situ* dynamic fracture experiment, for example. This was generally accomplished by lowering beam voltage and increasing deflection currents. At higher deflection currents the time allowed for imaging was restricted to reduce the possibility of over-heating the scan-coil assembly.

i. *perform experimental tests on high strength brittle materials including cement and concrete samples and examine the microstructural response at different levels of impulse.*

Initial tests were performed on rosin which is weak and brittle but has the desirable properties of transmitting a 1 μs wide pulse with little dissipation and of being able to fracture in a comparable time. Though this material is not strong or cementitious, we believe it may offer a useful model for brittle materials of higher strength.

Subsequent tests were performed on DSP cement mortar using a specially designed tension-compression loading stage. The loads are applied manually and, hence, can be considered static. However, after initiation of the crack the propagation is a dynamic phenomena and images of the crack propagation were obtained in real-time. Appendix A to this report discusses in detail the operation of the FSEM for these tests and it reports on limited analyses of the in-plane displacement of the crack tip using image processing methods. In addition, movies on a video tape of these tests have also been made.

j. *perform tests on selected ductile materials to find the response at the microstructural levels of such materials under high strain rate conditions.*

The *in situ* dynamic fracture experiments discussed above with a brass/rosin rod interface were a test of a ductile material--brass, as well as a brittle material--rosin. A movie of this test on a video-tape was made. As mentioned above, effects due to loading with the 1 μs pulse-width pressure pulse occurred too rapidly for the 381 Hz maximum framing rate capability of the microscope at present. However, the requirement for high strain rate is well met because the loading stresses were on the order of 1000-3000 psi/μs. We hope that with the addition of a brighter cathode and and scan generators capable of higher framing rates, observation of interesting dynamic microstructural response in such materials will be possible.

IV. Publications, Presentations and Patent Activity

Publications

1. B. H. Fishbine, R. J. Macy, T. J. Ross and M. L. Wang, "SEM Dynamic Microscopy," in Micromechanics of Failure of Quasi-Brittle Materials, S. P. Shah, S. E. Swartz and M. L. Wang, eds., Elsevier, 1990, p. 365.

2. B. H. Fishbine and R. J. Macy, "FSEM: Fast Scanning Electron Microscopy," Proceedings of XII International Congress on Electron Microscopy, Seattle, WA, August, 1990, San Francisco Press, 1990, p. 606.

3. B. H. Fishbine and R. J. Macy, "First Results With a High-Imaging Speed Scanning Electron Microscope," Reviews of Scientific Instruments, October 1991.

4. M. L.Wang, T. J. Ross, Z. L.Tan and R. J. Macy, "Fracture Study of Quasi-Brittle Material Using a Fast-Scanning Electron Microscope", to appear in Experimental Techniques, March 1991.

5. M. L. Wang, T. J. Ross, Tan, Z. L. and Macy, R. J. "Microfracture mechanism of a propagating crack in DSP cement mortar", submitted to Journal of Cement and Concrete Composites.

6. "High-speed secondary electron imaging in SEM with the Everhart-Thornley detector," working title, in draft.

7. "High-speed secondary electron imaging in SEM with CCD arrays," working title, in draft.

8. B. H. Fishbine and M. L. Wang, "Magnetically-Induced, One Microsecond Duration Pressure Pulses for Microscopic Dynamic Fracture Studies," to be submitted.

9. B. H. Fishbine, "A New Method for Magnetic Impulse Testing of Solids," to be submitted.

10. B. H. Fishbine, "An Impulse Compression/Tension Loading Technique for Microscopic Materials Strength Studies," to be submitted.

Presentations

1. "FSEM: Fast Scanning Electron Microscopy", Poster #11-31, Session: Advances in SEM Instrumentation, XIIth International Congress for Electron Microscopy, Seattle, WA, August 16, 1990, T. J. Ross.

2. "SEM Dynamic Microscopy," International Conference on Micromechanics of Failure of Quasi-Brittle Materials," Albuquerque, New Mexico, June 8, 1990, B. H. Fishbine.

3. "Fast Scanning Electron Microscopy for High Speed MicroCircuit Metrology and Inspection," SEMATECH, Austin TX--April 19, 1990, B. H. Fishbine.

4. Los Alamos National Laboratory Superconductivity Pilot Center--August 22, 1989, T. J. Ross, B. H. Fishbine and R. J. Macy

5. UNM Dept. Civil Engineering Graduate Student Seminar--September 13, 1989, T. J. Ross, B. H. Fishbine and M. L. Wang

6. New Mexico Research and Development Institute, Santa Fe, New Mexico--November 3, 1988, B. H. Fishbine and T. J. Ross

Patent Activity

1. Patent Pending: New Apparatus for Fast, Real-Time, Continuous Scanning SEM; Inventors: T. J. Ross, M. L. Wang, I. D. R. Mackinnon; Assignee: KACHINA Technologies, Inc.; Attorney: Samuel Freund, Los Alamos, NM (see DD Form 882, submitted to AFOSR, 10/15/90)

2. Patent Pending: Symmetric, Non-kinetic Magnetic Impulse Device; Inventors: T. J. Ross, B. H. Fishbine, M. L. Wang; Assignee: KACHINA Technologies, Inc.; Attorney: Samuel Freund, Los Alamos, NM (see DD Form 882, submitted to AFOSR, 3/28/88)

V. References

1. Phase II proposal to AFOSR SBIR Program, "Development of a High Imaging-Speed Scanning Electron Microscope for Dynamically Loaded Materials," Intelligent Systems Integration, 3/10/88.

2. B. H. Fishbine, R. J. Macy, T. J. Ross and M. L. Wang, , "Development of a High-Imaging Speed SEM for Dynamically-Loaded Materials," AFOSR Phase II SBIR Project Annual Report, IntelliSys Corporation, 10/27/89.

3. L. Reimer, Scanning Electron Microscopy, Springer-Verlag, 1985, p. 31.

4. See Reference 2.

5. Rod Norville, private communication.

6. B. H. Fishbine and R. J. Macy, "First Results With a High-Imaging Speed Scanning Electron Microscope," tentatively scheduled to appear in Oct. 1990 issue of Rev. Sci. Instrum.

7. B. H. Fishbine, R. J. Macy, T. J. Ross and M. L. Wang, "SEM Dynamic Microscopy," in Micromechanics of Failure of Quasi-Brittle Materials, S. P. Shah, S. E. Swartz and M. L. Wang, eds., Elsevier, 1990, p. 365.

8. B. H. Fishbine, "An Impulse Compression/Tension Loading Technique for Microscopic Materials Strength Studies," to be submitted to Rev. Sci. Instrum.

9. B. H. Fishbine, "A New Method for Magnetic Impulse Testing of Solids," to be submitted to J. Appl. Mech.

10. B. H. Fishbine, "Magnetically-Induced, One Microsecond Duration Pressure Pulses for Microscopic Dynamic Fracture Studies," to be submitted to J. Vac. Sci. Tech. B.

11. G. K. Lal and M. J. Hillier, "The electrodynamics of electromagnetic forming," Int. J. Mech. Sci. **10**, 491 (1968), for example.

12. F. Bauer, "Piezoelectric and electric properties of PVF_2 polymers under shock wave action: applications to shock transducers," in Shock Waves in Condensed Matter, J. R. Asay, R. A. Graham and G. K. Straub, eds., Elsevier, 1984, p. 225 and Kynar Piezo Film Corporation, P.O. Box 799, Valley Forge PA 19487.

13. F. C. Moon and S. Chattopadyay, "Magnetically induced stress waves in a conducting solid--theory and experiment," J. Appl. Mech. **41**, 641 (1974).

Appendix A

Operation of the FSEM and Loading Stage for Study of Fracture in Quasi-Brittle Material

Introduction

For quasi-brittle material, such as concrete, a significant amount of research has been conducted under the assumption that a process zone develops ahead of a crack tip. Here, a crack process zone is defined as a zone of distributed microcracks ahead of a macrocrack, in a region both above and below the plane of the macrocrack. The very existence of such a zone has recently been the subject of a major inquiry [1]. Experimental evidence [2, 3] seems to indicate that such a zone is extremely hard to identify. It is difficult to avoid the conclusion that the process zone is not a fundamental material property for cementitious materials, and it depends on specimen geometry and the method of measurement.

The most straight-forward experimental example involve Mode I cracks as developed, for example, in tension, or 3-point and 4-point bending tests. In addition to the apparent ductility displayed prior to the peak load, a softening branch of the load-displacement curve is exhibited in the post-peak load region. Under certain combinations of material and geometrical properties, cracks will propagate in a continuous, but slow-rate, under displacement control [4]. This suggests that the crack driving force is just sufficient to overcome the crack resistance and that the process is not necessarily unstable as is commonly claimed. Suppose for the moment that cracks may grow at the rate governed by an inherent material property and the crack driving force. Then if a specimen is loaded dynamically, the average stress could significantly exceed the static stress necessary to cause failure, and any number of pre-existing flaws could serve to initiate cracks. In the case of impulsive dynamic loads, the growth of these cracks in the matrix is soon arrested because of the short temporal character of the impulsive load. But, in the impulsive case, the matrix cracks can become concentrated at the interface with inclusions, and cracks can develop in the inclusions. Therefore, for the dynamic situation, it appears to be appropriate to talk of a microcrack process zone. To predict this evolution, the dynamic process associated with a single crack must be understood.

To acquire experimental evidence of this dynamic process, a fast-scanning electron microscope (FSEM) has been developed at the University of New Mexico. The FSEM is capable of >1 kHz framing rate, with the large depth of focus and high resolution which make SEM generally superior to light microscopes. Increasing framing rate by 10^1-10^4 times that presently available (so-called TV-rate--30-50 Hz) permits a variety of new dynamic microscopy studies. Specimens of high strength cement mortar were tested in the FSEM chamber in real-time to provide micrographs of the fracture process as it evolves in time. A special in-situ tension and compression stage was designed and fabricated for use in the dynamic microfracture studies.

Unlike conventional SEM, the FSEM has to sacrifice some depth-of-field and submicron resolution as the framing speeds increase. This is manifested in a reduced signal-to-noise ratio (S/N), where the image appears "snowy". The S/N ratio of the imaging signal is important in FSEM because at high digitizing rates the number of quanta in the imaging signal available to determine the contrast level of a pixel in the final image may be quite small. For example, for our typical scan beam current of 1 nA, only 31 electrons will strike the specimen in a digitizer sample time of 5 ns, corresponding to a digitizing rate of 200 MHz. An image correlation technique was developed to correct some of the deficiencies of a reduced S/N in order to measure the displacement distribution in front of the tip of the propagating crack. The results demonstrate that the proposed new FSEM and image techniques are a viable tool for moderate dynamic fracture studies of quasi-brittle and cementitious materials.

Fast Scanning Electron Microscope (FSEM)

Conventional SEM can obtain clear, sharp, static micrographs with large-depth-of-field and high resolution. This is typically done with scan times of tens of seconds, and sometimes even minutes. This long scan time is necessary to boost the signal-to-noise (S/N) ratio of the image. Put another way, increasing the dwell time (the time the electron probe is at a given point on the specimen) increases the number of detected secondary electrons (signal) being emitted from the specimen, thus resulting in better S/N and a good quality micrograph. This exceptional quality of conventional SEM micrographs is sacrificed to some extent with the FSEM. Our current FSEM, which uses a low-brightness Tungsten electron source, scans the sample at least an order-of-magnitude faster than TV rate and several orders of magnitude faster than typical micrographs are made. Fast scanning of the specimen results in fewer secondary electrons produced per unit time, and the resulting micrographs are a bit "snowy" when compared to typical SEM micrographs. However, the "snowiness" can be reduced with brighter electron sources and improved SE detection means. Hence, in FSEM there is a trade-off between image quality and scanning speed for a given electron source.

It is important to realize that though the wonderful sharpness of slow scan SEM images may be sacrificed as we reduce pixel resolution to increase framing rate in the FSEM, we will retain high spatial resolution and large depth of focus, and gain increased temporal resolution. A great deal of useful information can be extracted from the type of imaging available from enhancements in temporal resolution [5].

The FSEM acquires its signal digitally. The output of the SE detector is modulated, then processed by a high-speed (25 MHz) analog-to-digital (A/D) converter capable of digitizing very high band-width signals from the SE detector. Conventional SEM's record an image either on photographic film or video-tape. However, most conventional SEM's use analog storage which, at fast scan rates, will be unsatisfactory. Due to the speed of dynamic events of interest in the fracture mechanics discipline, real-time observations on a CRT are impossible. Our FSEM stores each frame on a personal computer hard disk for frame-by-frame playback at later times. Of course, having all the qualities of a conventional SEM and the capabilities of microsecond framing rates is highly desirable. Future research efforts are being focused in this direction. A short discussion of potential problems of imaging S/N and possible solutions in improving FSEM image quality will be described later. A schematical diagram of the FSEM system is shown in Figure 1.

Taking a "fast scan set" of snapshots involves first imaging the output of the high-speed ET detector on a high band-width CRT. This allows focusing, spot-size setting, specimen manipulation, gun-tilt adjustment, and other adjustments necessary to obtain a good FSEM image. When one is satisfied that there is a sufficient S/N ratio and the image is in focus, the ET detector output signal is switched to a high-speed A/D digitizer (LeCroy™ 8828D). The deflection generators are also switched from standard saw-tooth wave generators (used when viewing and focusing the image) to other generators synchronized with the clock of the digitizer. Finally, to begin a digitizing sequence of frames, the LeCroy system must either be manually triggered or triggered in response to a dynamic initiating event (such as a microfracture).

The digitized signal is transferred from the digitizer's fast-memory to the hard disk of a microcomputer for image processing and frame-by-frame viewing. The final product with the present FSEM system is 16 frames of 256x256 pixels at 381 Hz framing rate (25 MHz pixel rate). This pixel rate is approximately 2 times faster than any previously reported SEM digital imaging system [6]. Other details on this system and potential application areas other than dynamic microfracture are given in [5].

SEM Tension-Compression Stage

Figure 2 shows our tension-compression (T-C) stage which mounts to the FSEM's x-y-z position stage. A single sliding brass threaded block moves in a machined aluminum body assembly. To accommodate various materials, a variety of fixtures may be mounted to the moving block. To provide rotation of the lead-screw, a worm and ring gear (40:1 ratio) setup is utilized. This greatly reduces reverse rotation and provides a smooth application of lead-screw torque.

A square shaft slides in a keyed slot running through the worm gear and a 90 degree bevel gear system with another square free sliding shaft connects through a Delrin™ U-joint to a vacuum rotational-feed-through shaft. This shaft can either be rotated by hand, or it can connect to a geared stepper motor, for precise feed-back control.

Using the T-C Stage with a wedge driver, there is a need for a right-hand threaded lead-screw and one moving block . The wedge is attached to the block and the notched specimen is held by a "C-clamp type bracket" that is secured to the back plate on the T-C stage. This specimen mounting greatly reduces rigid body motion. Changing the lead screw to one which has half left hand and half right hand threads, and adding another block with left hand internal threads, converts our single ended T-C stage to a double acting stage. Turning the rotary shaft one way will slowly move the blocks apart, and turning the shaft the other way will move the blocks together.

The T-C stage design discussed above represents a very accurate method of applying mechanical loads without going to very expensive precision roller-bearing systems.

Trigger Design and Circuitry

Capturing an event of interest necessitates synchronizing the start of an event with the digitized 16-frame movie sequence described above. At our current framing rate (presently 381 frame per second) each frame is ~2.5 milliseconds, therefore the entire 16-frame movie represents a 40 millisecond time segment. Triggering the digitizer too early or too late will result in missing the event (microcracking, etc.). Detecting the time of cracking in cement was first attempted using a piezo-electric transducer. However, it was difficult to discriminate (electronically) between the acoustic pulses from failure and pulses from friction due to "wedge-rubbing" against the notch of the cement specimen.

For now, a direct mechanical solution to triggering has been used. A crack-detector (CD) gauge consisting of a single strand of high endurance alloy is used. Local fracture of the sensing strand will occur with the propagation of a crack beneath the gauge, as shown in Figure 3. Similar to a strain gauge, the crack detector is epoxied to the surface of the specimen. In our notch-wedge tests the CD gauge is epoxied just below the notch and perpendicular to it, again as shown in Figure 3. The CD gauge has two alloy pads with a 0.020 inch wide foil joining them. Soldered to the pads are two copper wires which are connected to a standard vacuum electrical feed-through, allowing a connection between the cement specimen in vacuum in the FSEM chamber and the outside of the chamber.

A small bias current is applied to the CD gauge and the voltage is sensed by a comparator circuit, as seen in Figure 4. When the CD gauge is intact, the voltage across the gauge is very low (the resistance of the gauge is only a few ohms), but when the CD gauge fails the voltage across the gauge goes "high". The change in voltage activates a comparator circuit which in turn "pulls" the +5 volt LeCroy™ trigger level to ground, triggering the digitizer movie sequence.

The response time of the electronics, i.e.(comparator circuit, LeCroy™ trigger circuit) is typically < 1 microsecond. The response time of the CD gauge however is in question. Mounting, type of epoxy used on the surface, and surface preparation all are probably important, as they are with strain gauges.

Test Procedure

Notched densified-small-particle (DSP) cement mortar specimens were placed and secured to the loading stage using the clamp and set screw arrangement described above. These specimens had a 28-day compressive strength of about 9,000 psi. Magnification was adjusted, using deflection voltage and accelerating voltage, so as to image the entire width of the notch as well as the field just in front of the notch. Once the notched area of the specimen was imaged and focused on the viewing CRT, successive stages of increasing loading were applied. The wedge was advanced by turning an external loading control, slowly stressing the sample in stages. The loading control was sensitive enough so that the beginning of loading could be felt easily and the gear-reduction was large enough that the sample could be loaded to failure with very little torque applied to the loading control.

Once the macrofracture process was initiated the macrocrack propagated very rapidly, although not faster than the FSEM framing speed. At each successive stage of loading a digitized movie was taken with the FSEM. Typically five to ten 16-frame sequences were taken for each specimen from a condition of no load to failure.

The specimen is mounted and loaded using the T-C stage as discussed above, and field-of-view and focusing adjustments are accomplished using the viewing monitor. However, instead of stages of loading, the specimen is loaded all the way to failure with continuous loading. The digitizing movie sequence is initiated by the electrical opening of the CD gauge (the propagating crack breaks the CD gauge) which is epoxied to the specimen in such a location as to ensure that the macrocrack will propagate through the gauge. Results of the above test procedure are manifested in a 16-frame sequence of micrographs over a 40 millisecond time period of crack growth (at 2.5 milliseconds per frame).

Requirements to Improve Images

Without the use of a brighter cathode, improvements to the S/N ratio at present framing rates may be accomplished by enhancements to the detection system. More work needs to be done to determine if all of the signal secondary electrons are being detected and what effect the very high count rates are having on the signal detection and amplification electronics. The literature on high-speed photon counting indicates that counting, rather than integrating pulses, can give an increase in the S/N ratio [6]. Possible parallel multiple detectors to handle very high count rates also may improve the S/N ratio.

There are other ways to increase S/N: increase the primary electron beam voltage (V), increase the half-angle subtended at the specimen (α), increase the beam diameter (probe diameter) at the specimen (d_p), or maximize $g(\Phi,T_c) \equiv T_c e^{-\Phi/kT_c}$ (where Φ is the work function of the cathode surface material, k is a constant, and T_c is cathode temperature). Increasing V, α, or d_p may, however, interfere with specimen observation: some specimens are altered or destroyed by high beam voltage; increase of α reduces depth of focus; increase of d_p reduces spatial resolution. Maximizing $g(\Phi,T_c)$ by increasing T_c may dramatically shorten tungsten filament life, for example. Maximizing $g(\Phi,T_c)$ by reducing Φ is a more flexible option, as the widespread use of LaB_6 and increasing use of ZrO/W cathodes [7] have shown. Also, field, thermal-field or photoemission processes can dramatically improve cathode brightness. For the first FSEM experiments, we were able to explore several high-imaging speed issues without using advanced cathodes; our success with the tungsten hairpin cathode encourages us to continue experiments using higher brightness cathodes. Depending on operating parameters, LaB_6 and ZrO/W cathodes may offer brightness improvements ot 10-1000 times over that of the tungsten hairpin cathode.

Image Correlation Technique for Displacement Measurements

With the resolution restrictions of the current FSEM system, image processing of the micrograph data can be used to enhance the image quality and the associated data analysis. In micromechanics problems, the spatial scale over which the crucial deformation is inhomogeneous falls between 0.1 and 100 microns. This is below the resolution of most (Moire' interferometry techniques can now be resolved to 0.1 micron displacement detail [8]) traditional experimental techniques. To experimentally investigate a variety of micromechanics deformation problems, a method, called digital cross-correlation, can be used to determine the displacement fields generated by mechanical load by comparing a pair of SEM micrographs, one recorded before the load is applied and the other after load application [9-12]. The displacements are measured by cross-correlation analysis of the relative positions of visible surface texture on the micrographs. The cross-correlation algorithm is based on using a two-dimensional Fast Fourier Transformation (FFT) approach. Reduction of the noise effect on the micrographs also improves the accuracy of displacement measurements between the strained and unstrained sub-images of the SEM micrographs.

A schematic illustration of this digital image processing approach is shown in Figure 5. The cross-correlation algorithm was developed and built into a microcomputer system. This algorithm divides one image (256x256 pixels) into subsets (32x32 pixels). An image can be from both deformed and undeformed specimens. Each subset was chosen large enough so that its light intensity pattern does not resemble any other subset in the image, i.e. the subset intensity patterns must be unique. After the image from an undeformed specimen is analyzed, a second image (usually from a deformed specimen) is searched for the location which most resembles the light intensity pattern of the first image. This is done to provide some correlation between subsets of the images. A two-dimensional FFT was used to find this correlation. A discrete correlation of two images is defined as follows:

$$\Phi(k, l) = \sum_{i=0}^{M-1} \sum_{j=0}^{N-1} I_A\,(i-k, j-l) \cdot I_B\,(i, j) \tag{Eq. 1}$$

where $\Phi(k, l)$ is the correlation coefficient between subset image intensities k and l, which are located at Cartesian coordinates x_k and y_l, and $I_A(k, l)$ is the intensity of pixel (k, l) in image A and $I_B(i, j)$ is the intensity of pixel (i, j) in image B. The parameters M and N are chosen as follows:

$$\begin{aligned} M &\geq C + D - 1 \\ N &\geq E + F - 1 \end{aligned} \tag{Eq. 2}$$

where $I_A(i, j)$ and $I_B(i, j)$ are discrete arrays of size CxD and ExF, respectively. This is required for avoiding "wrap-around" error in the period of the correlation function. Since correlation theory holds as

$$C(k, l) \Leftrightarrow I_A^{*}(u, v)\ .\ I_B(u, v) \tag{Eq. 3}$$

where $I_A^{*}(u, v)$ denotes the complex conjugate of $I_A(u, v)$ in the spatial frequency domain, and (u, v) are the spatial frequency components.

The computation of the cross-correlation is often more efficiently carried out in the frequency domain using FFT techniques. We first compute the cross-correlation of the two sub-images for both undeformed and deformed specimens. This results in a correlation whose peak location is the offset of these two sub-images. The peak intensity position is then interpolated to subpixel accuracy by fitting a parabolic surface to a 3x3 neighborhood centered at the pixel having maximum intensity. For example, Figure 6 and Figure 7 are the 32x32 subsets of images from the undeformed and deformed specimens, respectively. The pixel density ranges from 0 to 255. Figure 8 is the correlation of Figures 6 and 7. The autocorrelation function of Figure 6 is also shown in Figure 9. To obtain the displacement, two peak intensity positions of Figure 8 and Figure 9 are compared; the differences in position determines the displacement.

Noise Effect

A low pass filter was used to reduce the noise present in the images. For example, a line across an image from 0 to 255 pixel with associated intensity is shown in Figure 10. High frequency noise was obviously present in the image. With the application of low-pass filters, the smoothed light intensity across the line is shown in Figure 11.

For a 32x32 pixel sub-image, the smoothed image intensity after applying the low-pass filter is shown in Figure 12. So far we have demonstrated the use of a low-pass filter to smooth the image across only one direction, but the same procedure was used to smooth the image across the other orthogonal direction. For example, Figure 13 is a smoothed version of a 32x32 sub-image of Figure 6. This filter procedure was done to improve the accuracy of the obtained displacement field.

In summary, in order to obtain the displacement of the sub-images, for undeformed and deformed specimens, we first use a forward FFT of these two sub-images, and apply the spatial low-pass filter to smooth the images. Second, we multiply the resulting transform by the complex conjugate of the other as demonstrated in Eq. 3, and third, we use the inverse FFT to transform back into the spatial domain. For example, a micrograph of a specimen deformed immediately after and during the crack initiation is captured is shown in Figure 14. This micrograph was compared with the micrograph of the undeformed specimen (which is not shown in the diagram) to obtain the displacement in front of the crack tip. The resulting displacement in front of the crack tip in the x and y directions are shown in Figures 15 and 16, respectively. The total resultant displacement is shown in Figure 17 and this figure was used to determine the displacement field as shown in Figure 18. A rigid-body motion in the y-direction was detected in the loading process as shown in this figure.

Conclusions

A fast -scanning electron microscope has been developed. It is capable of framing rates of 381 hz which allow the capture of microstructural changes in a dynamic event. An in-situ tension and compression stage was designed and fabricated for use in the dynamic microfracture studies of cementitious materials. Fast scanning of the specimen results in fewer secondary electrons produced per unit time, and the resulting micrographs are snowy when compared to typical SEM micrographs. However, the snowy micrograph can be improved with brighter electron sources and improved SE detection. An image correlation technique was also developed to reduce the noise in order to measure the displacement in front of the tip of the propagating crack. Compact tension specimens of DSP cement mortar were tested inside the SEM chamber by means of a tension and compression stage. A crack-detector gauge consisting of a single strand of high endurance alloy was used to trigger the recording sequences. Results of the experiment are a 16-frame sequence of micrographs over a 40 millisecond time period of crack growth (at 2.5 milliseconds per frame). The displacement distribution around the propagating crack was obtained using an image cross-correlation method. Displacement components and rigid body motion during loading were obtained. The rigid body motion provided a way to calibrate and redesign an in-situ loading stage.

References for Appendix

1. Mindess, S. (1990), The fracture process zone in concrete, proceedings of NATO Advanced Research Workshop: Toughening Mechanisms in Quasi-Brittle Materials, S. Shah (ed), Northwestern University, Evanston, IL, 335-350.

2. Wang, M., Schreyer, H. and Rutland, C. (1990), Internal deformation measurements with the use of real time x-rays, Micromechanics of Failure of Quasi-Brittle Materials, Shah, S, Swartz, S. and Wang, M. (eds), Elsevier Science, London, 81-94.

3. van Mier, J. (1990), Internal crack detection in single edge notched concrete plates subjected to uniform boundary displacement, Micromechanics of Failure of Quasi-Brittle Materials, Shah, S, Swartz, S. and Wang, M. (eds), Elsevier Science, London, 33-42.

4. Tasdemir, M., Maji, A. and Shah, S. (1990), Crack propagation in concrete under compression, J. Eng. Mech., 116, 5, 1058-1076.

5. Fishbine, B., Macy, R., Ross, T. and Wang, M. (1990), SEM Dynamic Microscopy, Micromechanics of Failure of Quasi-Brittle Materials, Shah, S, Swartz, S. and Wang, M. (eds), Elsevier Science, London, 365-374.

6. Hayashi, T., Photomultiplier Tubes For Use In High Energy Physics, Application RES-0791-02, Hamamatsu TV Co. LTD.

7. Gesley, M. (1989), Thermal-field-emission electron optics for nanolithography, J. Appl. Phys., 65, 914.

8. Epstein, J. (1985), Dynamic Moire interferometry in mechanics research, proceedings 3rd Symp. Energy Eng. Sciences, Penn State University, College Park, PA, 155-166.

9. James, M., Morris, W. and Cox, B. (1990) A high accuracy automated strain-field mapper, Experimental Mechanics, 30, 60-68.

10. Peters, W. and Ranson, W. (1982) Digital image technique in experimental mechanics, Optical Engineering, 21, 3, 427-431.

11. Russell, S. and Sutton, M. (1989), Strain-field analysis through correlation of x-ray radiographs of a fiber-reinforced composite laminate, Experimental Mechanics, 237-340.

12. Davidson, D. (1990), Micromechanics of materials brittle at ambient temperature, Micromechanics of Failure of Quasi-Brittle Materials, Shah, S, Swartz, S. and Wang, M. (eds), Elsevier Science, London, 305-314.

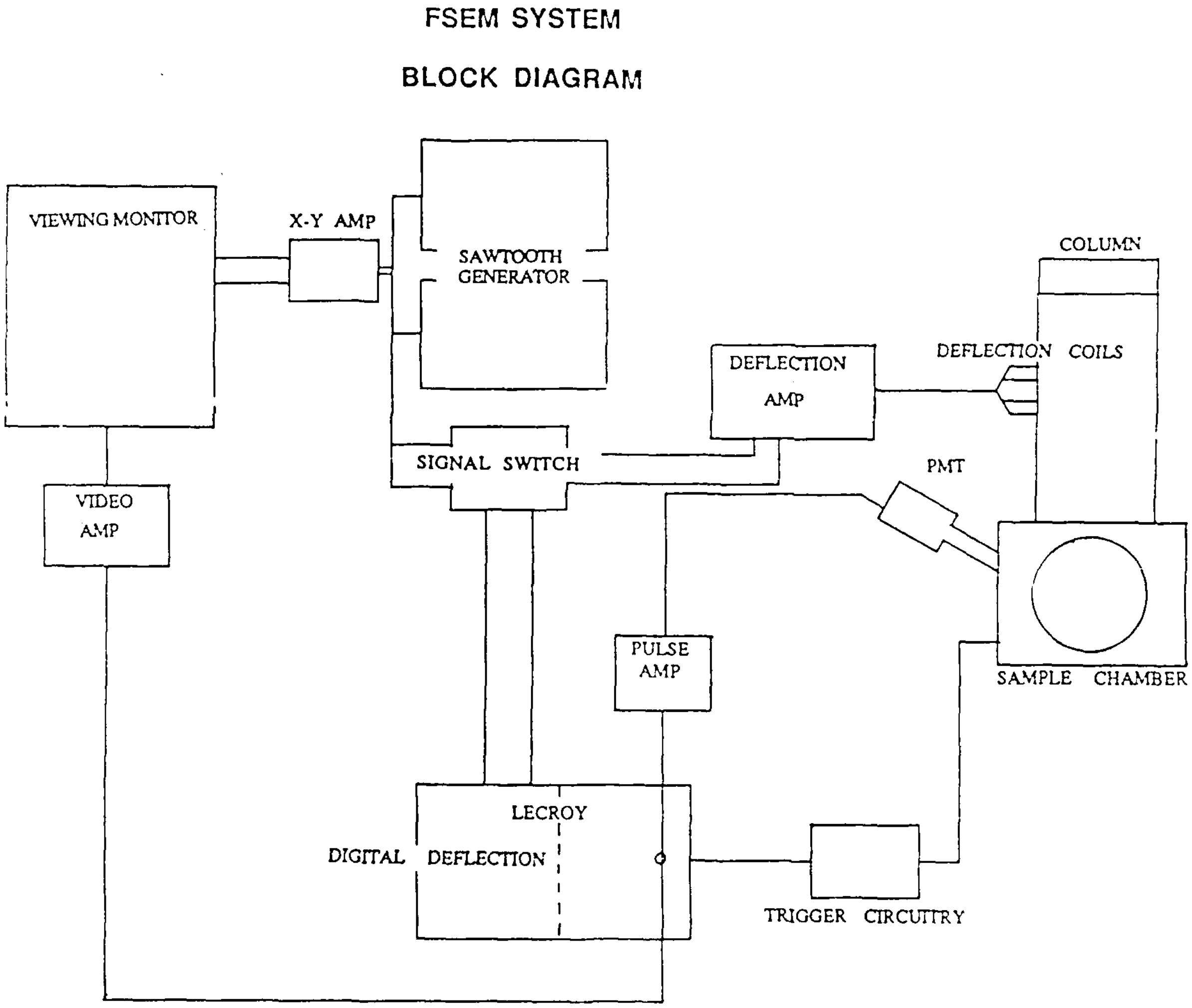

Figure 1. Schematic Diagram of the SEM.

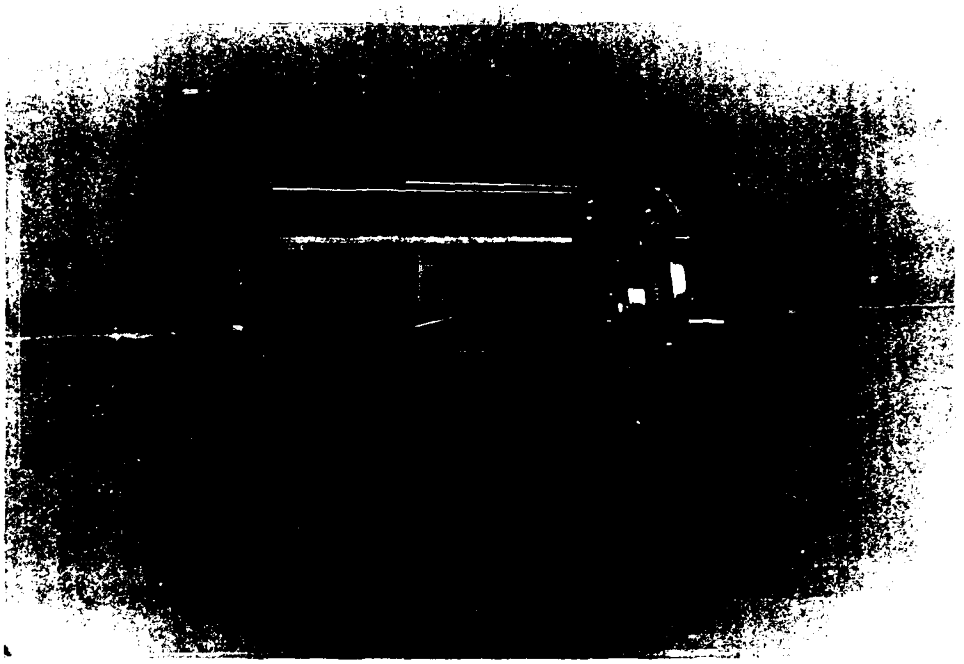

Figure 2. Tension- Compression Loading Stage Mounted to FSEM.

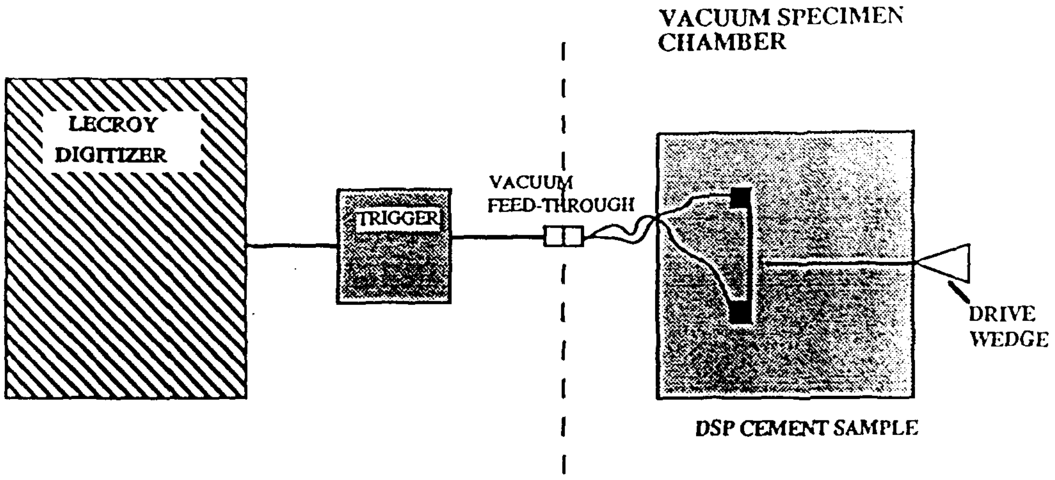

Figure 3. Crack Detection Gage and Sensing Device.

CRACK DETECTION TRIGGER CIRCUITRY

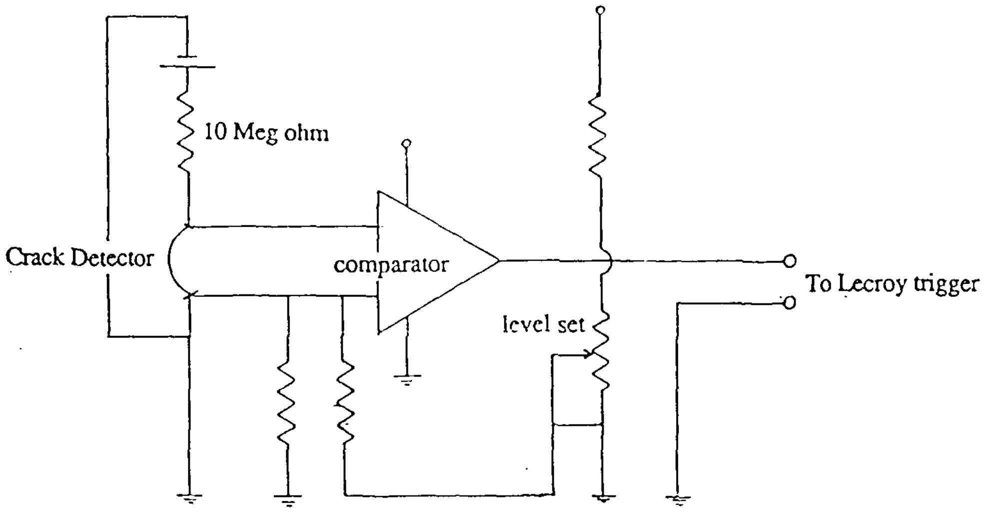

Figure 4. Crack Detection Trigger Circuitry.

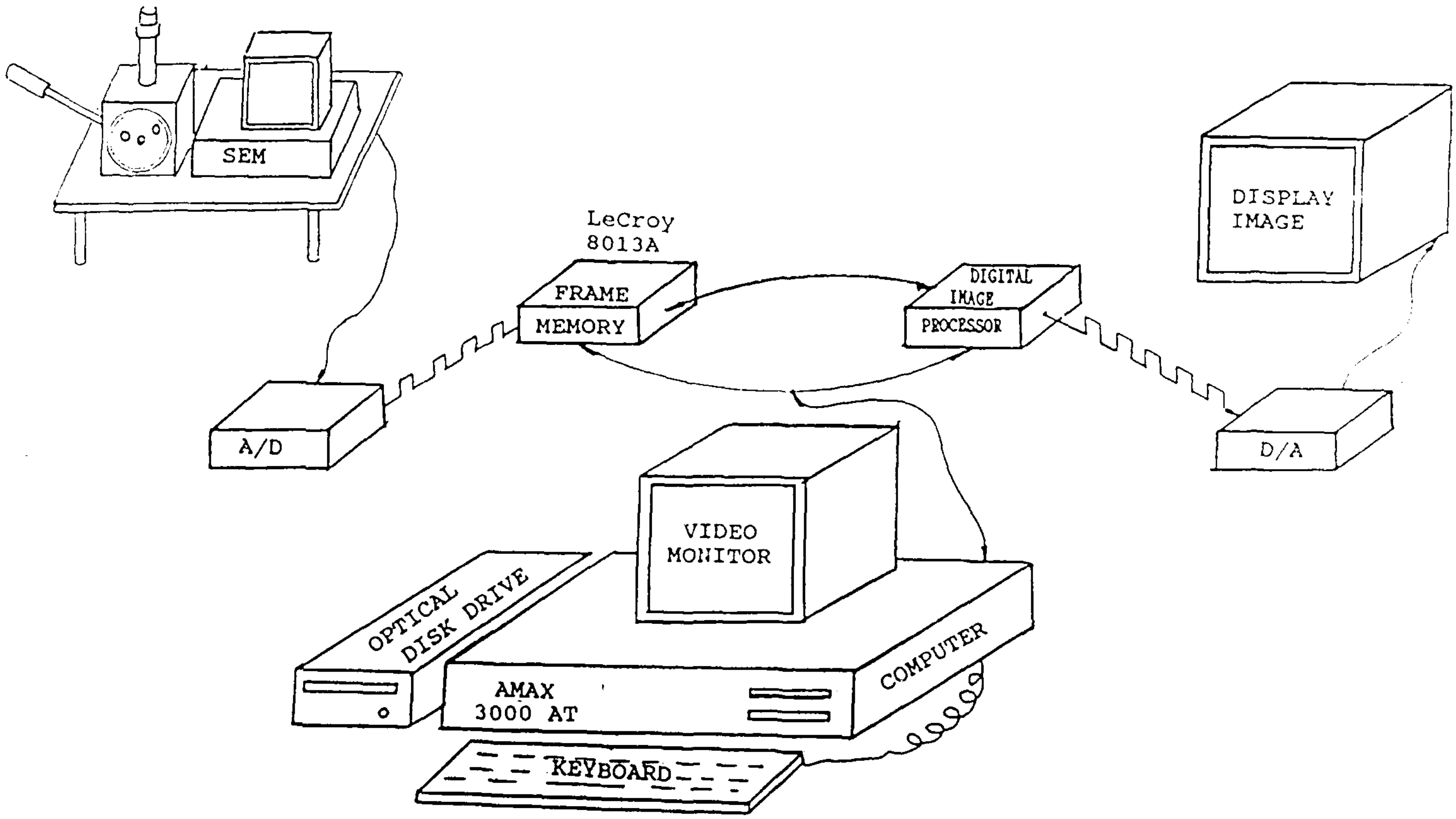

Figure 5. Schematic Illustration of a Digital Image Processing Unit

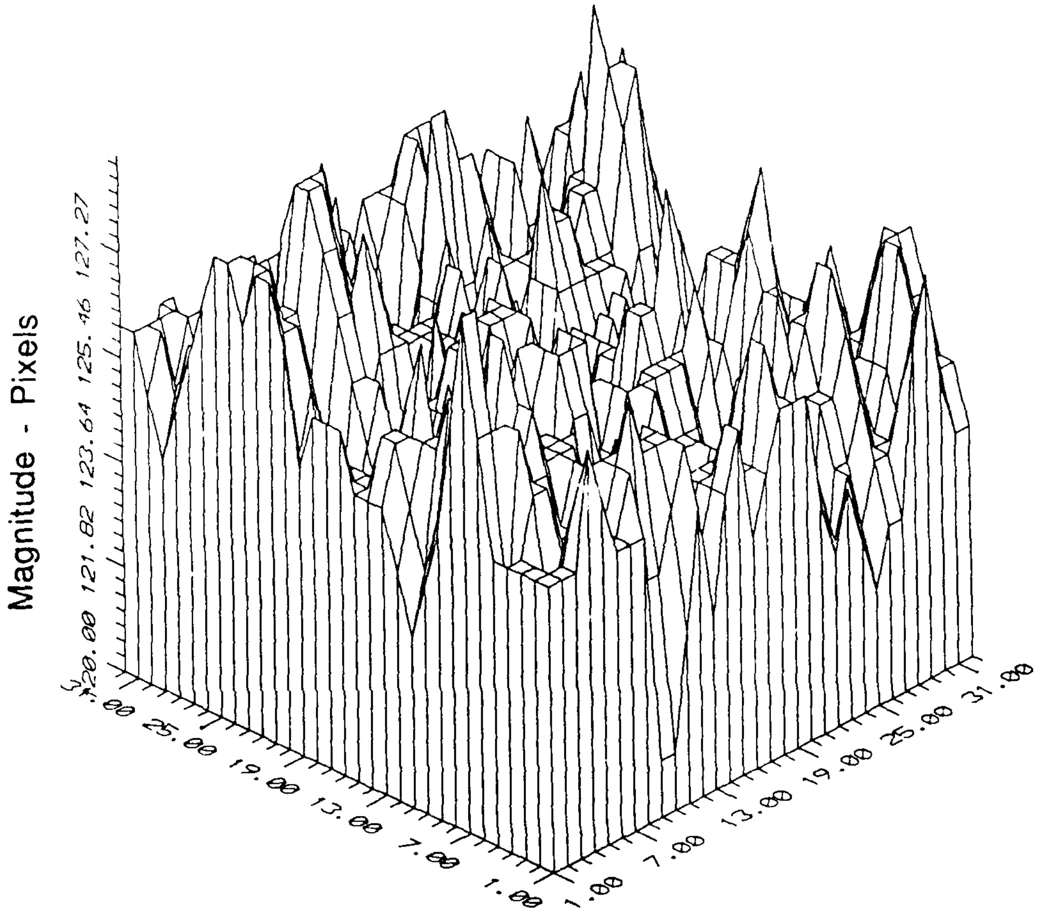

Figure 6. Undeformed 32 x 32 Pixel Subimage.

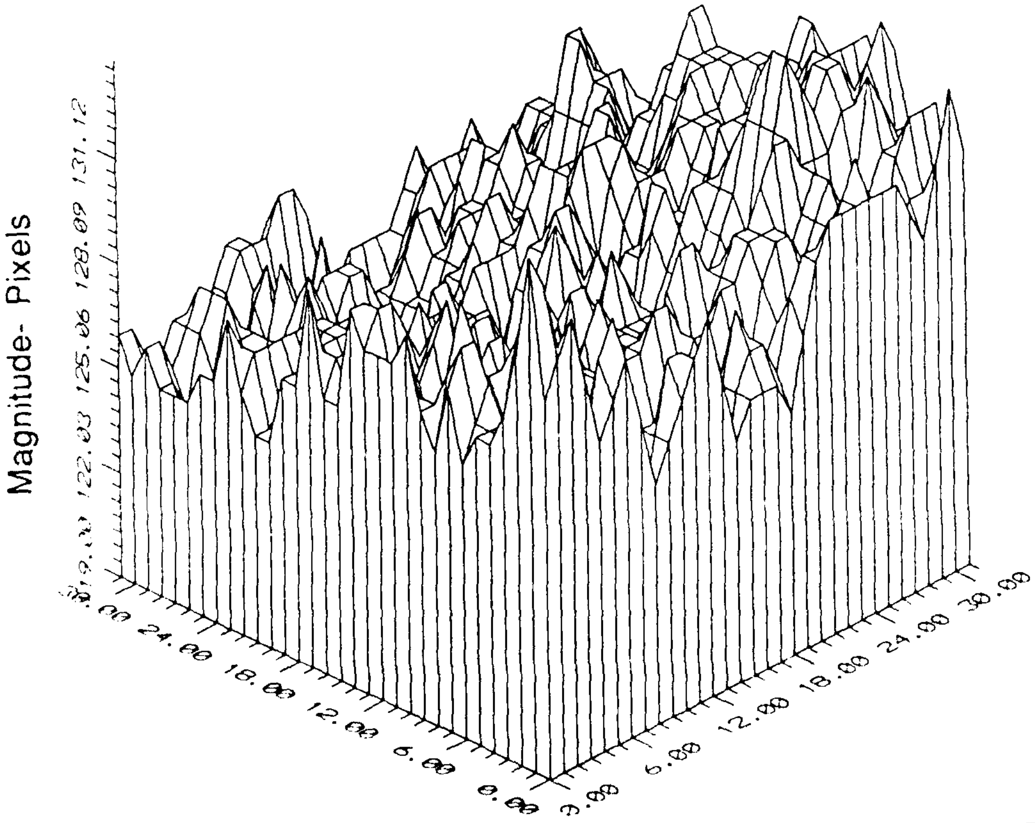

Figure 7. Deformed 32x32 pixel subimage as compared to Fig. 6.

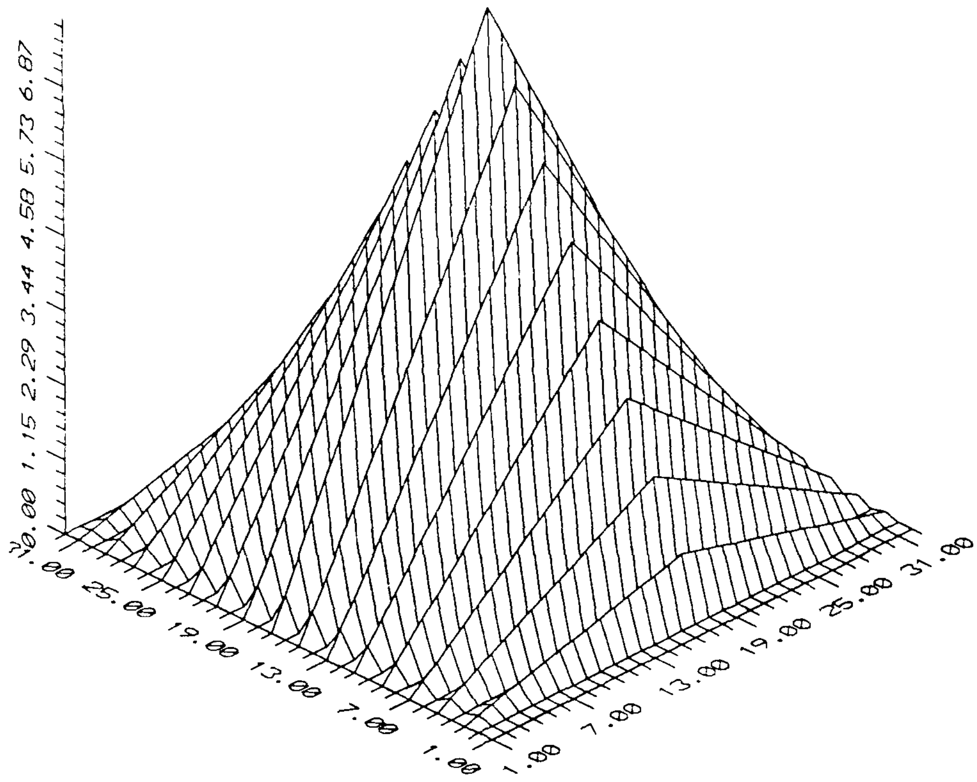

Figure 8. Cross- Correlation of two subimages (Figs. 6 and 7).

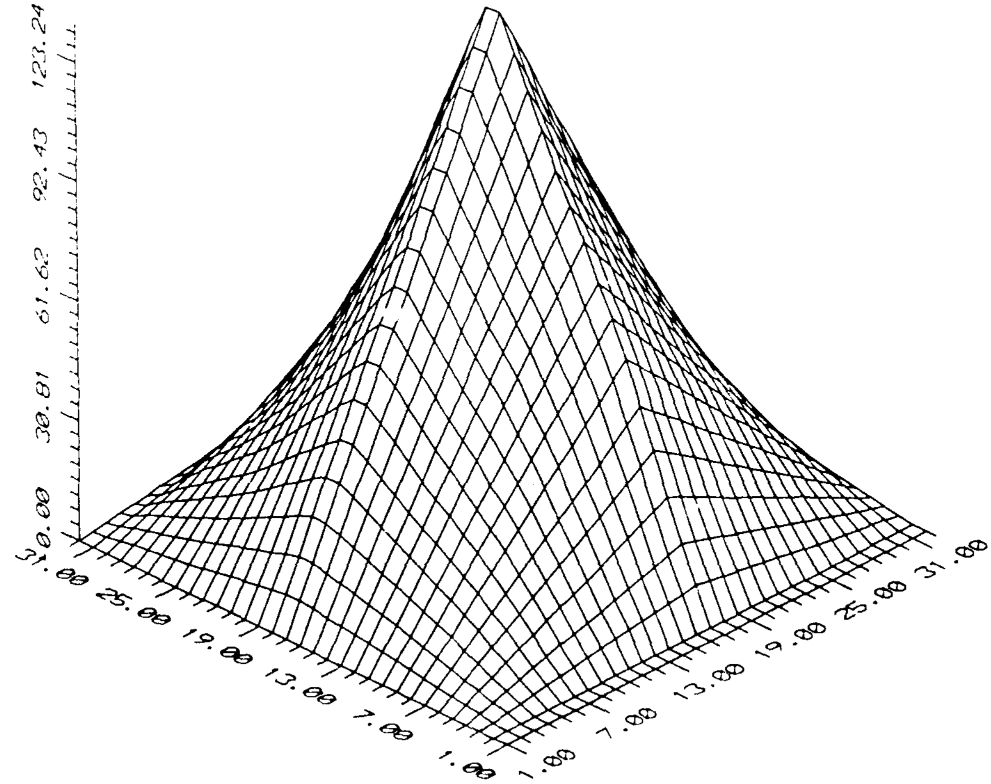

Figure 9. Autocorrelation of subimage (Figure 6.).

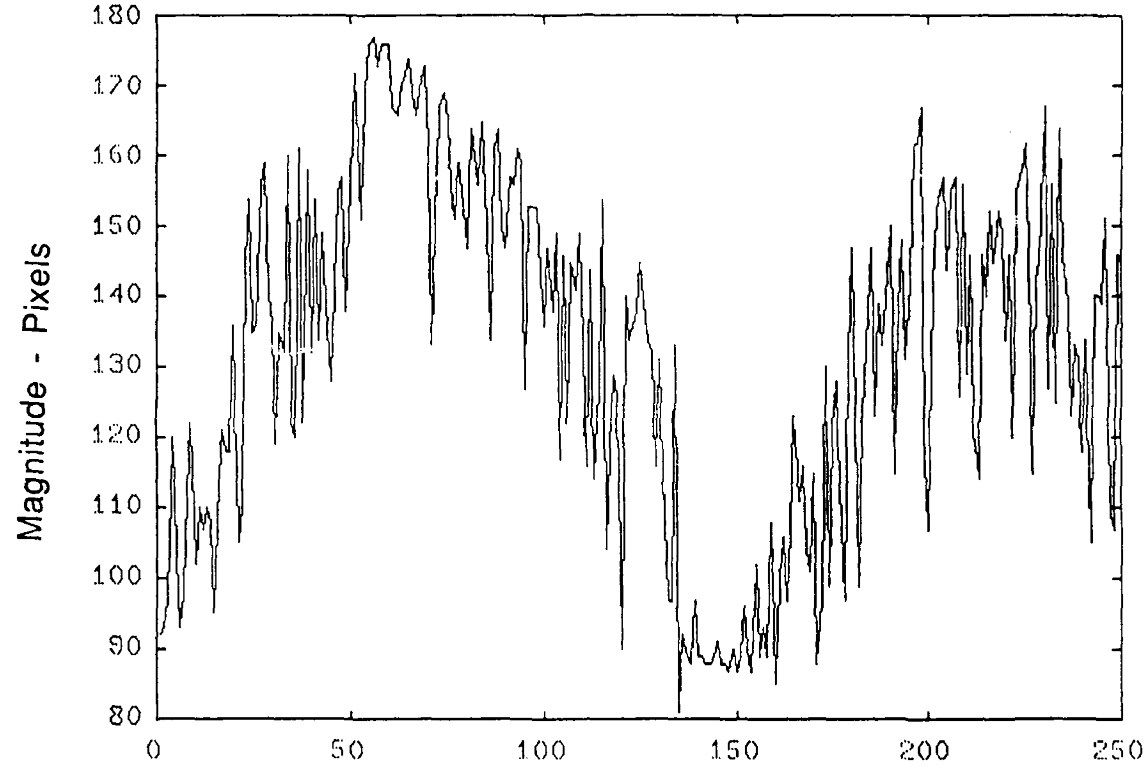

Figure 10. Intensity of a Line Across An Image.

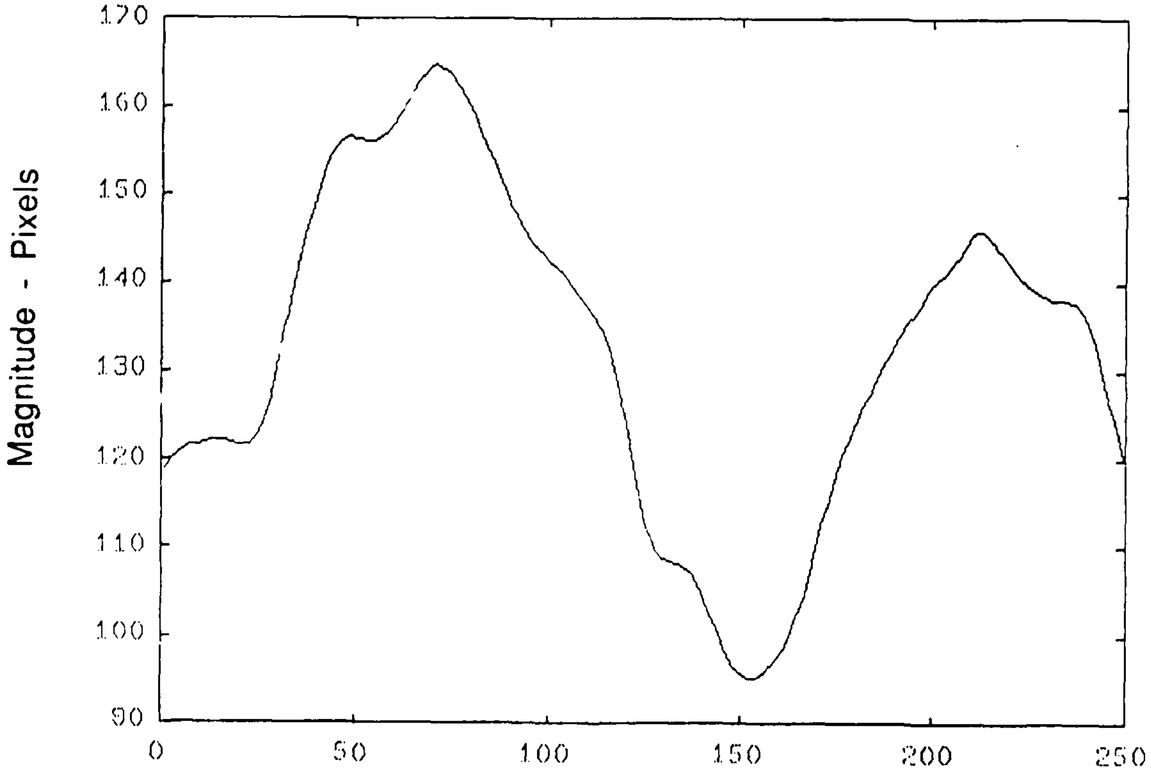

Figure 11. Intensity of a Line (Fig. 10) After the Application of A Low Pass Filter.

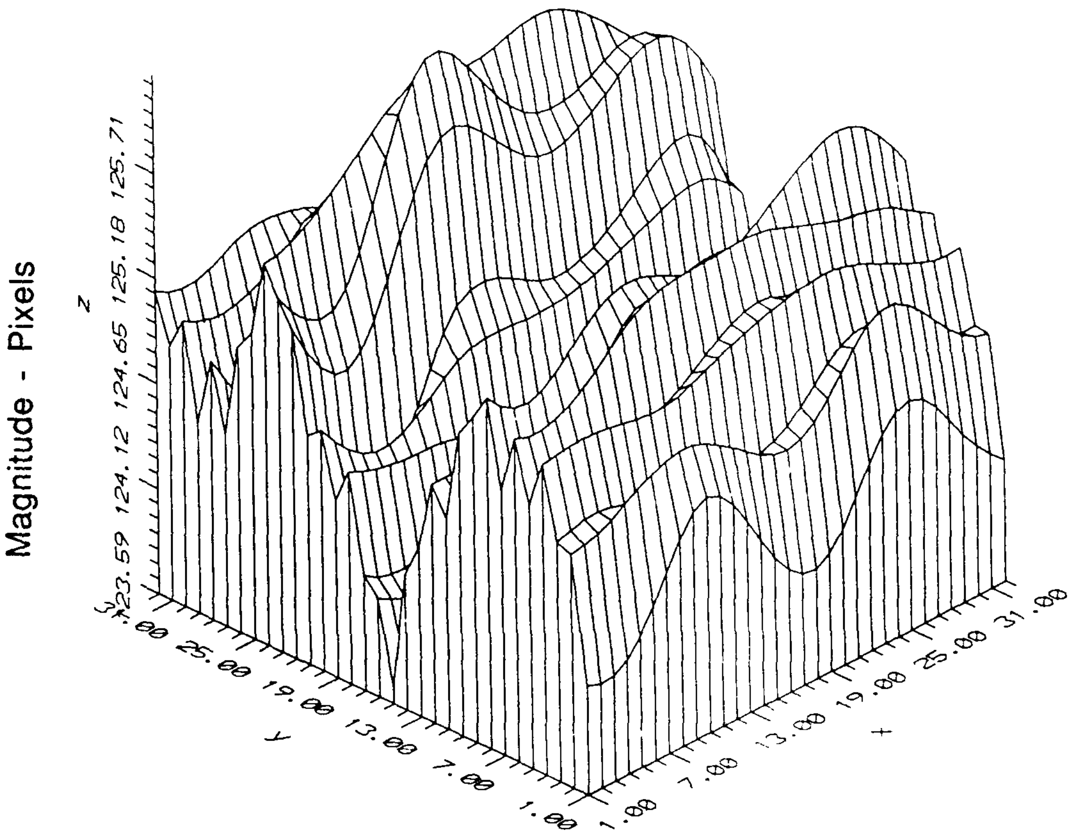

Figure 12. Smoothed Data of an 32x32 Subimage.

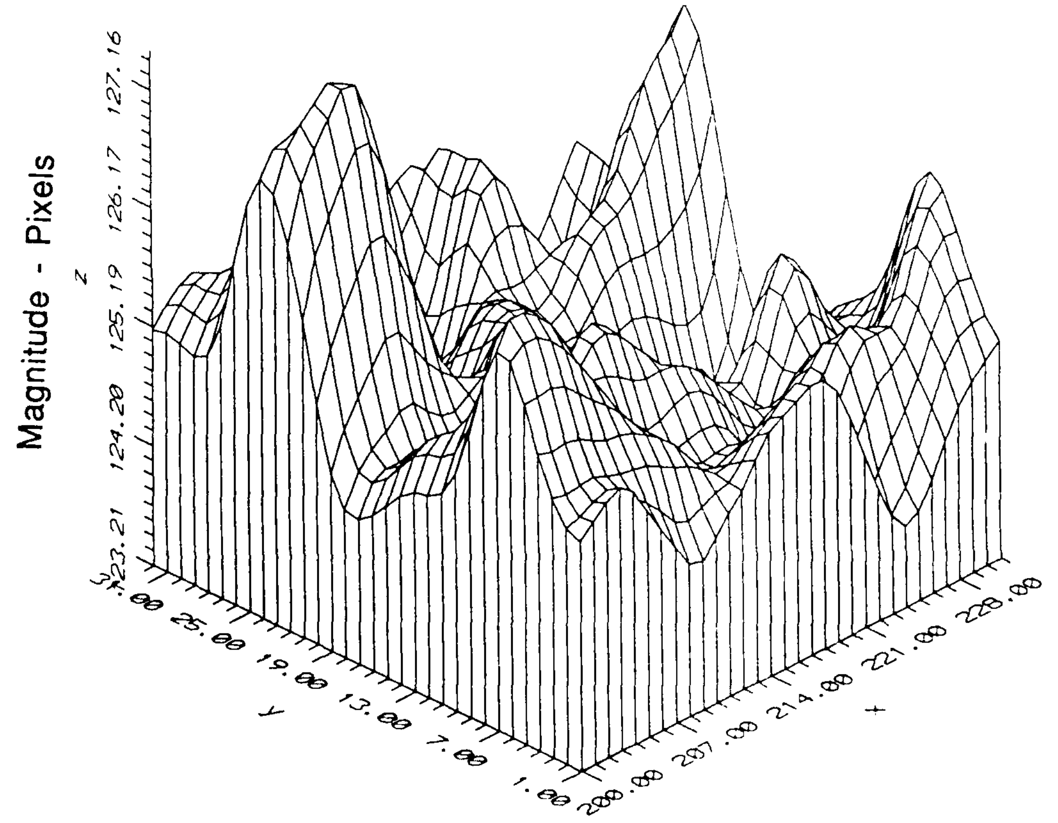

Figure 13. Smoothed Image of 32x32 Subimage of Figure 6.

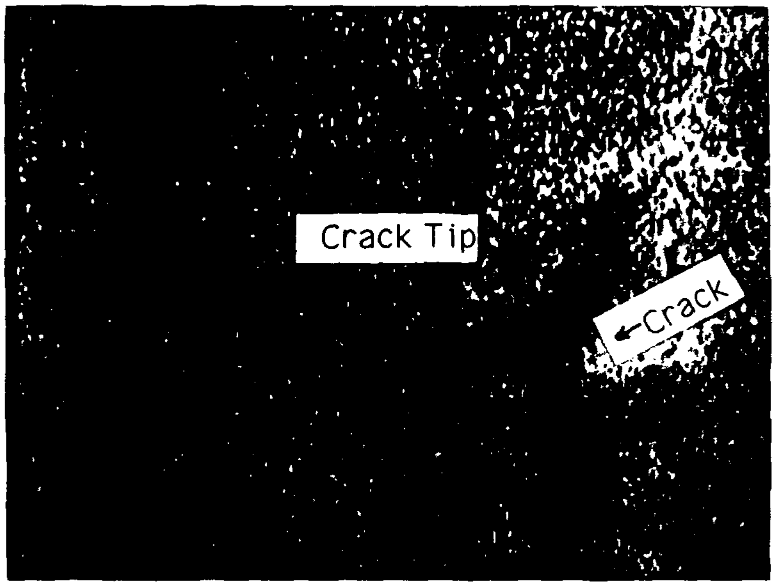

Figure 14. Micrograph of a Crack in DSP Cement Mortar.

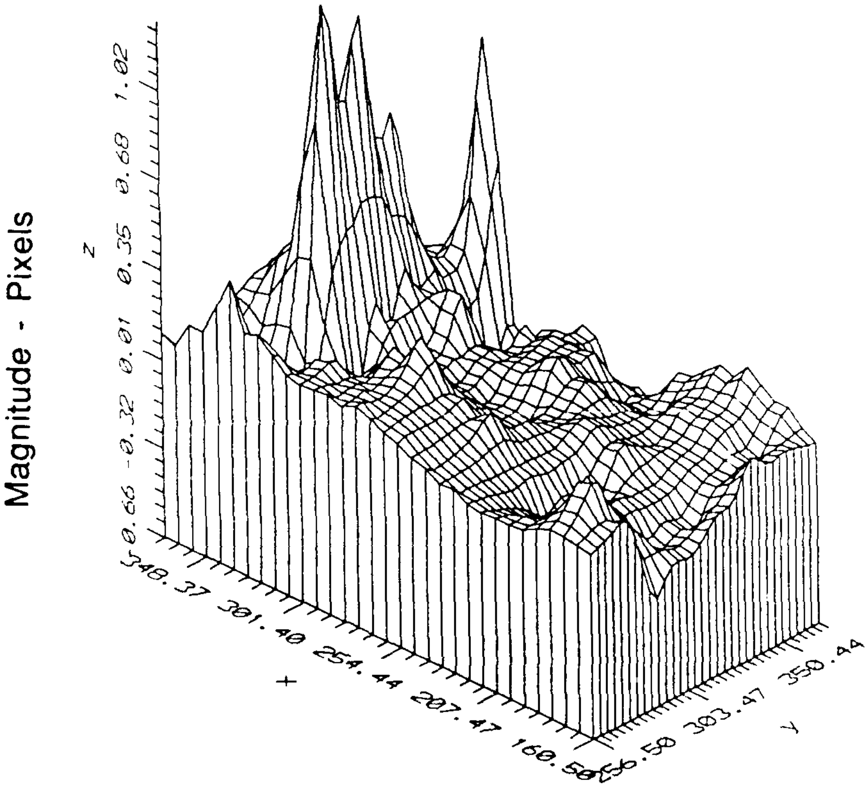

Figure 15. Resulting Displacement Immediately After Crack Initiated in X

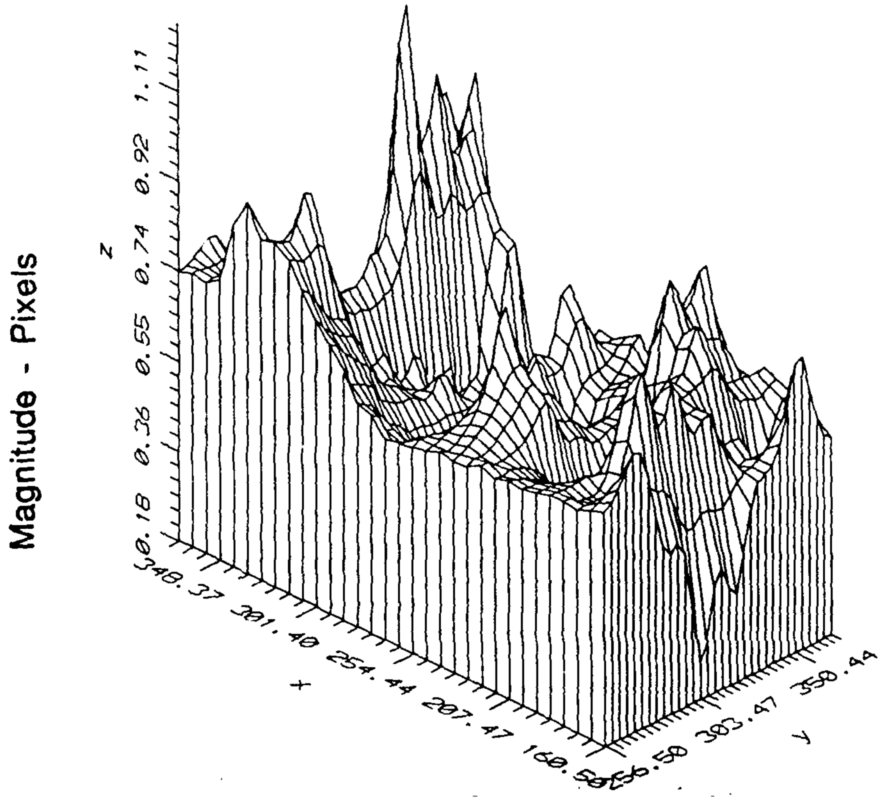

Figure 16. Resulting Displacement Immediately After Crack Initiated in Y

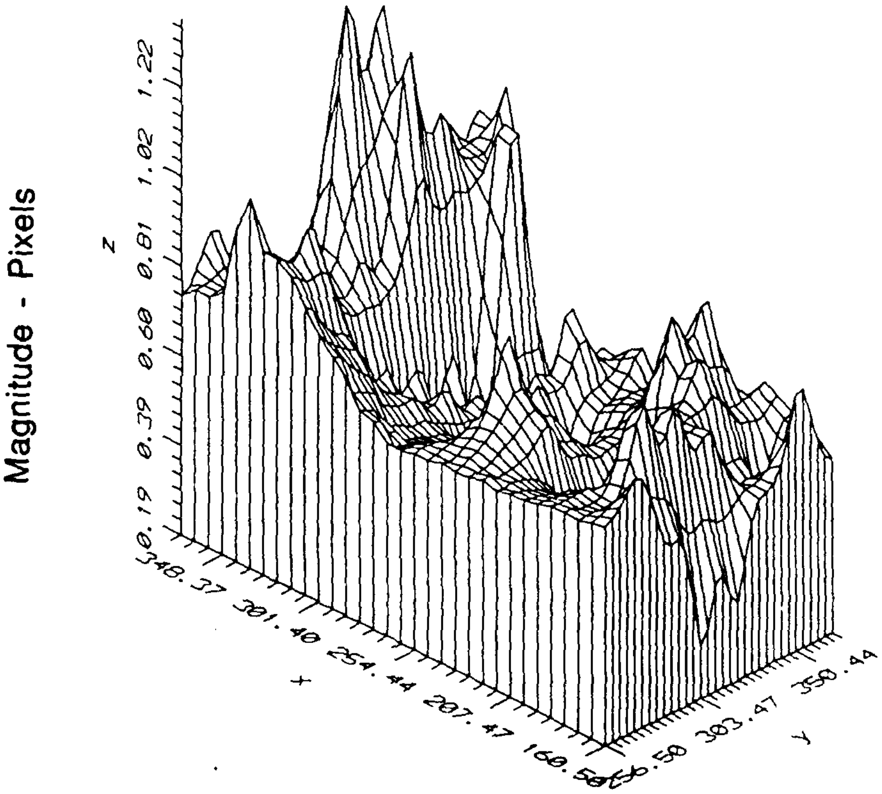

Figure 17. Resultant of Displacement.

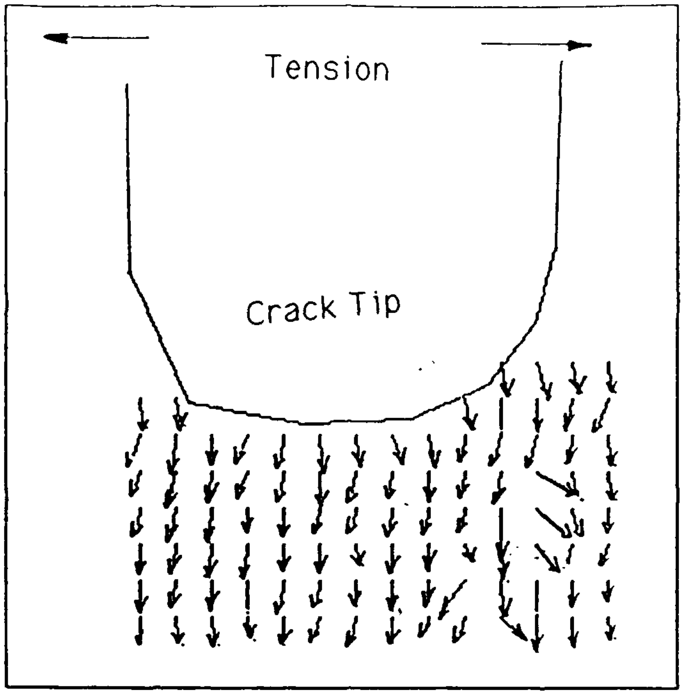

Figure 18. Displacement Distribution in Front of a Crack Tip.